

THE **MACH** INITIATIVE

THE MACH INITIATIVE PROPULSION REPORT

Romesh Thayalan (Candidate 12476)

Group Business & Design Project

University of Bath Department of Mechanical Engineering

Thursday 25th May 2023

Word Count: 5868



Summary

The preliminary design of the propulsion system for a high-speed RC aircraft was carried out with the aim of providing sufficient thrust at all stages of flight to reach Mach 0.8 (272 m/s) at sea-level. The different propulsion system types available were compared, including propellers, ducted fans, pulse jets, and turbojets. Using a thermodynamic marching model, calibrated with manufacturer data, turbojets were found to provide the dynamic thrust required for such speeds. The available turbojets were then ranked based on the thrust relative to estimated drag values, size, weight, as well as cost. A Pugh matrix approach was then used and the JetCat P300 was selected. The principal concern for the fuel system was the avoidance of engine air bubble ingestion. After consultation with Callen-Lenz, and considering the system employed by the current world record holder, a pair of fuel bags were selected. These are drained of air before being filled and do not ingest air as they are emptied. A Universal Air Trap (UAT) was employed as a mitigation in the event there are any remaining air bubbles. A ground station was also developed, including an external fuel pump, air pump, and reservoir to fuel the aircraft through the startup sequence, and drain it of fuel and air after each run. An inlet was designed to decelerate the high Mach number flow to an appropriate value at the compressor face for optimal thrust performance at Mach 0.8. For integration purposes, an s-duct was chosen. To achieve an efficient diffusion to the target Mach number, an inlet area of 2100 mm² was determined and a capture ratio of 0.75 was used for an adequate balance between low and high-speed performance. The length of the duct was a compromise of integration and optimal pressure recovery and distortion at 324 mm. The inlet shape is a rounded rectangle to remove any curvature reflexes on the external body and separate the internal secondary structures. A steady-state RANS model was set up, using the $k-\omega$ SST turbulence model, to analyse and optimise the duct. A total pressure ratio of 0.987 and a Radial Distortion Index (RDI) of 1.19% were achieved at the Aerodynamic Interface Plane (AIP).

Acknowledgements

My thanks go to Prof Carl Sangan for supervising The Mach Initiative. I would also like to thank Andy Walbridge, and Wojciech Wasinski, of Callen-Lenz, who sponsored the project, for their advice and feedback on our designs. A large aspect of this work would not have been possible without the generosity of Siemens in providing me with a license for STAR-CCM+. To my teammates, it has been a pleasure working with you all.

I thank my sister, Rachael, and my father, Dr Aingarapillai Thayalan, for their continuous support and welcoming me with open arms when I came home. Special thanks to Ponnoe, Ranjini, and Ruben Jeyasundaram, and Meera Urban; Gnanaraj, Vasanthi, Shiran and Shiromee, and countless others for their help in our time of need. To Rajvinder Meetca, I could not have done this without you.

Most of all, I thank my late mother, Dr Sumathy Thayalan (5th August 1962 – 28th December 2022), who is finally at peace.

Contents

Summary.....	1
Contents.....	3
<i>..... PART I: INTRODUCTION & CONCEPT SELECTION</i>	
<i>.....</i>	<i>7</i>
1.1 Introduction	7
1.2 Requirements & Key Design Objectives	7
1.3 Initial Concept Generation	8
1.3.1 Propulsion System Selection	8
1.4 Engine Selection	13
1.5 Inlet	15
1.5.1 Inlet Type	15
1.5.2 Inlet Sizing.....	16
1.6 Fuel System	18
1.7 Further Development Plan	19
<i>..... PART II: DETAILED DESIGN</i>	
<i>.....</i>	<i>20</i>
2.1 Fuel System Redesign	20
2.2 Nozzle	21
2.3 Inlet CFD Analysis	22
2.3.1 Computational Model	22
2.3.2 Limitations and Errors in the Computational Model	25
2.3.3 Results and Updates to the Inlet Geometry	26
2.3.4 Quantification of Distortion [30, 33].....	27
2.4 Future Work	30
2.4.1 Validation of the Thrust Models	30
2.4.2 Fuel System Ground Testing	31
2.4.3 Alternative Fuels	31
2.4.4 Thermal Modelling	31
2.4.5 Inlet Testing and Improved Modelling	31
2.5 Conclusion.....	32
2.6 Project Overview	32
2.7 References	33
<i>..... APPENDICES</i>	
<i>.....</i>	<i>34</i>
3.1 Appendix A – Turbojet Decision Matrix	34
3.2 Appendix B - General Assembly Drawing	35
3.3 Appendix C - Nose & Ballast Sub-Assembly Drawing	37
3.4 Appendix D - FWD Camera Mount Part Drawing	39

List of Figures

Figure 1. Control volume around a streamtube containing the actuator disc [3].	9
Figure 2. Variation of thrust with speed for propellers with sensitivity to input power and propeller diameter..	10
Figure 3. Schematic diagram of a turbojet [6].	11
Figure 4. Thrust against speed for the JetCat P400-PRO.	12
Figure 5. Layout concepts generated with the selected version boxed - featuring a double-delta and twin tail fins [1].	12
Figure 6. Thrust and drag at different wing loadings against speed for the JetCat P400. Dashed lines represent drag values.	13
Figure 7. Weighted total thrust performance against static thrust for JetCat and Behotec engines.	14
Figure 8. Weighted ranks for (a) Thrust-to-drag, (b) Thrust-to-area, (c) Thrust-to-weight, and (d) Cost against static thrust.	15
Figure 9. Comparison of vector flowfields for side mounted, fuselage-shielded, and wing-shielded at an incidence of 15° [16].	16
Figure 10. Sideview of s-duct showing external inlet profiles recovering to the rear fuselage.	17
Figure 11. Schematic of the s-duct in sideview with the key dimensions labelled.	17
Figure 12. Total pressure recovery and flow distortion at the AIP against axial length-to-AIP diameter ratio [18].	18
Figure 13. Kevlar fuel tank for the first iteration of the aircraft [1].	19
Figure 14. Schematic of the fuel system.	20
Figure 15. Ratio of gross thrust of a De Laval nozzle to a converging nozzle against NPR. N.B. $\gamma = 1.333$ was the value used for analysis purposes [2].	21
Figure 16. CFD flow domain and mesh structure inside the main duct.	22
Figure 17. Sideview schematic section of the s-duct showing the AIP and CF.	22
Figure 18. SAAB unstructured mesh with a virtual extension of the duct past the AIP to a mass-flow outlet [25].	23
Figure 19. Inflation layers in a generic CFD domain.	24
Figure 20. AIP Average Mach number against iteration for (a) Grid 1 and (b) Grid 2.	25
Figure 21. Total pressure ratio for iteration 1 inlet. (a) sideview of the centre plane. (b) front view of the AIP.	26
Figure 22. Iteration 1 streamwise vorticity (a), and total pressure ratio (b) at a plane 100 mm upstream of the AIP.	26
Figure 23. Total pressure ratio for iteration 2 inlet. (a) sideview of the centre plane. (b) front view of the AIP.	27
Figure 24. Iteration 2 streamwise vorticity (a), and total pressure ratio (b) at a plane 100 mm upstream of the AIP.	27
Figure 25. Instrumentation for measuring distortion [16].	28
Figure 26. Schematic of positions for monitoring distortion at the AIP. Dashed lines are the measurement locations, and solid lines are the physical duct and engine starter walls.	28
Figure 27. Total pressure against angular position for each ring plotted for both iteration 1 and iteration 2. The average value for each ring is also shown.	29
Figure 28. Radial total pressure distortion (a) and distortion extent parameter (b) against non-dimensional radius.	30

List of Tables

Table 1. Requirements that pertain to the propulsion system.	7
Table 2. Contradiction matrix for the current world record solution.	8
Table 3. Propeller configurations tested using the ADT dynamic model.	9
Table 4. Summary of station numbers and their meanings for a turbojet engine.	11
Table 5. Decision matrix used to select the turbojet for the aircraft. Note that the model name denotes the static thrust. See Appendix A – Turbojet Decision Matrix, for the values for each engine.	14
Table 6. Key dimensions of the iteration 1 s-duct.	18
Table 7. Grid independence study.	24
Table 8. Summary of the radial positions to monitor distortion.	28
Table 9. Distortion metrics for Iteration 1 and Iteration 2.	30

List of Symbols & Acronyms

Symbol	Meaning
RC	Remote Controlled
GWR	Guinness World Record
TMI	The Mach Initiative
GBDP	Group Business Design Project
ADT	Actuator Disc Theory
V	Velocity
A	Area
C_P	Power coefficient
P	Power
ρ	Density
C_T	Thrust coefficient
F	Thrust
BET	Blade Element Theory
EDF	Electric Ducted Fans
F_N	Net thrust
\dot{m}	Mass flowrate
U	Velocity
p	Pressure
NPR	Nozzle Pressure Ratio
η_j	Nozzle isentropic efficiency
γ	Ratio of specific heats
SAF	Synthetic Air Fuel
D	Drag
M	Mach Number
CF	Compressor Face

AIP	Aerodynamic Interface Plane
PDR	Preliminary Design Review
UAS	Unmanned Air Systems
UAT	Universal Air Trap
CFD	Computational Fluid Dynamics
IV	Intravenous
y^+	Non-dimensional normal wall distance
y	Normal wall distance
N	Total number of inflation (prism) layers
RANS	Reynolds Averaged Navier-Stokes
k	Turbulent kinetic energy
ω	Specific turbulent dissipation rate
SST	Shear Stress Transport
ε	Turbulent dissipation rate
URANS	Unsteady Reynolds Averaged Navier-Stokes
PC	Personal Computer
$(\Delta P_R / \Delta P)$	Radial total pressure distortion
RDI	Radial Distortion Index
θ	Distortion extent parameter
θ	Angular position
r/R	Non-dimensional radial position
HPC	High Performance Computing
FYP	Final Year Project
GA	General Assembly

List of Subscripts

Subscript	Meaning
e	Exit
a	Ambient
1	Compressor entry face
2	Compressor exit
3	Turbine entry
4	Turbine exit
5	Nozzle exit
g	Combustion gas property
t	Throat
c	Capture plane
c1	First cell
BL	Boundary Layer

PART I: INTRODUCTION & CONCEPT SELECTION

1.1 Introduction

For many years, remote controlled (RC) aircraft enthusiasts have been building and flying models to create the fastest one. As technologies have developed, the hobbyist has access to more complex components pushing this record higher. This has culminated in the current Guinness World Record (GWR) being set in 2017 by Niels Herbrich, who flew his aircraft to a speed of 465 mph – Mach 0.62.

The Mach Initiative (TMI) aims to surpass this record using engineering analysis and design principles. The propulsion system of such aircraft forms a key part of this goal, providing the thrust necessary to overcome the high drag seen in the high subsonic regime. It must be effective both in this condition, but also at low speeds during take-off and ground-running.

This report is split into two parts. Part 1 details the initial concept generation and selection of the propulsion system, while Part 2 concerns the detailed analysis and development of each subsystem.

1.2 Requirements & Key Design Objectives

To define project goals, formal requirements were agreed, categorised as:

- GWR requirements to satisfy that the aircraft and record attempt are valid.
- Regulations to ensure the aircraft is safe and able to fly in suitable airspace.
- Mission requirements.
- Needs of users including those setting up, flying, recovering, and maintaining the aircraft.
- Logistics.

They were then classified as either “**shall**” or “**should**”. A “shall” requirement is critical to the system’s operation, whilst a “should” is desirable but not necessary. Requirements which are salient to the propulsion system are shown in Table 1. A comprehensive list of the requirements of the project can be found in the Project Manager’s report [1].

Table 1. Requirements that pertain to the propulsion system.

Reference	Requirement	Category	Classification
R1	Maximum true airspeed > 404 kts (465 mph)	Mission	Shall
R2	Maximum Mach number > Mach 0.8 (272 m/s at sea-level)	Regulations	Should
R3	Generate all thrust using air-breathing engines , except for an initial impulse during take-off	GWR	Shall
R4	Net-zero CO ₂ emissions	Mission	Should
R5	Started and launched within 3 hours of being unloaded at a test range	User	Shall
R6	Batteries and liquid propellant removable from airframe	User	Shall
R7	Batteries and liquid propellants charged / loaded on test range	User	Shall
R8	Batteries and liquid propellants discharged / unloaded on test range	User	Shall

From these requirements, the key objectives can be derived:

- [R1-R3] – Enough thrust must be generated to reach Mach 0.8
- [R1-R3] – Enough energy must be stored to complete the entire record attempt.
- [R3] – Flights should be carbon neutral.
- [R5-R8] – The system must be serviceable whilst embedded in the aircraft.

1.3 Initial Concept Generation

To generate concepts, the TRIZ method was employed as described in [1]. This involved identifying the ten core functions of the aircraft and noting Herbrich's solutions. The impact made by increasing each value (where applicable) on each of the functions is marked as positive, negative, or having no effect.

The current solution employs a 180 N class turbojet engine fuelled with Jet-A1 kerosene. This is fed to the engine from a repurposed hydration pack via a fuel pump and filter. Five contradictions were identified as shown in Table 2, coming from the weight penalty of increasingly powerful turbojet engines and their high cost and complexity.

Table 2. Contradiction matrix for the current world record solution.

Reference	Function Contradicting With	Contradiction Description
C1	Take-Off	Increased weight leads to higher required take-off speed
C2	Recovery (Landing)	Increased weight leads to higher required landing speed
C3	Remain Controllable During Flight	Increased thrust increases acceleration of vehicle and off-axis thrust moment
C4	Affordable (<£20k)	Turbojets are high cost (of the order of £5,000)
C5	Manufacturable	Turbojets require many ancillary systems (e.g. fuel pumps, filters, fuel tanks)

1.3.1 Propulsion System Selection

Solutions to resolve these contradictions were generated from the alternative propulsion types available. Some options, such as pulsejets and adding an afterburner to a lower power turbojet, were discarded due to feasibility. The availability of pulsejets has diminished significantly with most now entirely custom-built, which is outside the scope of a GBDP. Similarly, an afterburner, which is highly complex to design on its own, would require an accompanying variable area nozzle for maximum benefit [2], ruling this out.

1.3.1.1 Propellers and Ducted Fans

Propellers were considered, as they can be driven by electric motors which would achieve the aim of net-zero flight emissions. To estimate their dynamic performance, a propeller was modelled using Actuator Disc Theory (ADT). This assumes that the propeller is an infinitely thin disc, with radially uniform thrust distribution [3]. In addition, the linear theory of lift is assumed throughout, and the propeller's induced velocity is contained entirely

in a streamtube surrounded by stationary air [4]. A control volume is defined with freestream flow at speed V_0 , exit velocity V_e , and a disc of area A as Figure 1 shows.

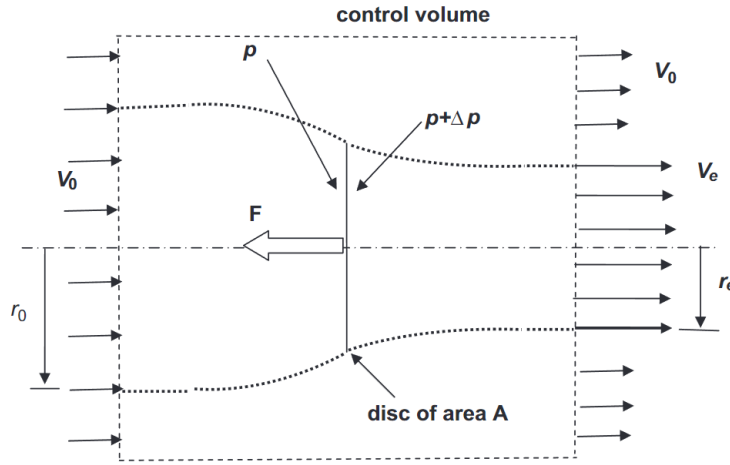


Figure 1. Control volume around a streamtube containing the actuator disc [3].

From Sforza [3], the power coefficient, C_P , is defined by

$$C_P = \frac{P}{\frac{1}{2} \rho A V_0^3}, \quad (1)$$

where P is the power driving the propeller, and ρ is the air density. The thrust coefficient, C_T , is given by the thrust, F , through

$$C_T = \frac{\frac{F}{A}}{\frac{1}{2} \rho V_0^2}. \quad (2)$$

They can then be related to one another by

$$C_P = \frac{1}{2} C_T (1 + \sqrt{1 + C_T}). \quad (3)$$

A propeller system from the fastest propeller driven RC aircraft was used to define the power input and the disc area. Using a 4800 W motor and a 12 in diameter propeller, which gave a disc area of 0.073 m², C_P was found for a range of speeds using Equation (1). The corresponding C_T value was determined from Equation (3) and the thrust calculated from Equation (2). To assess the sensitivity to the input power and diameter, each of these were doubled independently relative to the baseline, giving the configurations shown in Table 3.

Table 3. Propeller configurations tested using the ADT dynamic model.

Configuration Number	Name	Input Power (W)	Propeller Diameter (in)
1	Standard	4800	12
2	Power Sensitivity	9600	12
3	Diameter Sensitivity	4800	24

Figure 2 shows a precipitous reduction of thrust with speed for all configurations. Increasing the propeller diameter raises static thrust. However, this asymptotically tends to the baseline case. Increasing the power input has an influence at all speeds, but its effect is minimal at higher velocity.

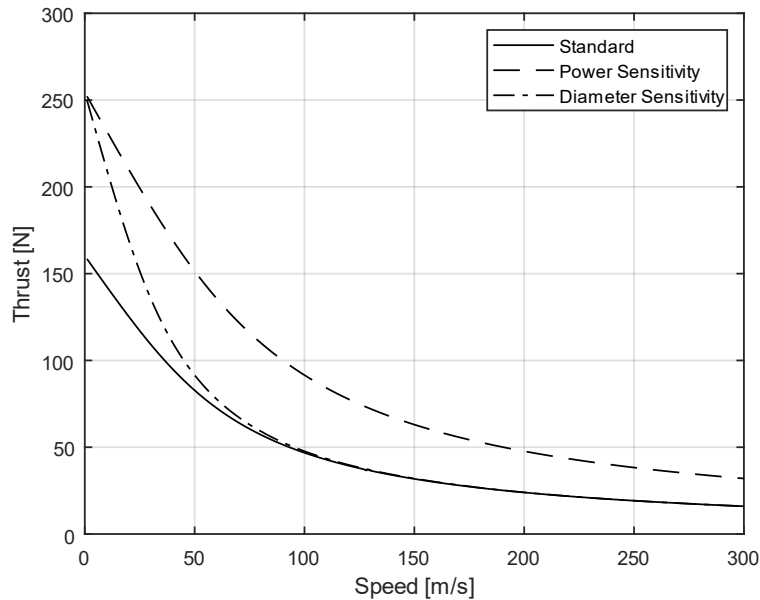


Figure 2. Variation of thrust with speed for propellers with sensitivity to input power and propeller diameter.

The preliminary drag models predicted a drag of approximately 160 N at Mach 0.8 [5]. With suitably sized motors or internal combustion engines having power in the range of 5-8 kW, the thrust developed would not be sufficient to reach the design speed, so open propellers are not suitable for the aircraft.

ADT does not consider the effect of the blade tip-vortices, which draw out flow from the streamtube meaning the induced flow is lower than predicted [4]. Blade Element Theory (BET) can be modified to account for this. However, since the thrust is overpredicted and still shows that propellers are insufficient for the design, it is not necessary to improve the model further.

Electric Ducted Fans (EDF) reduce losses by suppressing the formation of tip-vortices as the blades are just able to clear the duct [3]. However, this only approaches the results of ADT and the most powerful EDF commercially available has a static thrust of 250 N. From Figure 2, this would not give sufficient thrust to reach Mach 0.8.

1.3.1.2 Turbojets

To model the performance of turbojet engines, a 1-D marching analysis was performed (see [6]) for an example engine – the JetCat P400. Figure 3 shows the layout of a generic turbojet alongside numbers which pertain to the stations shown in Table 4.

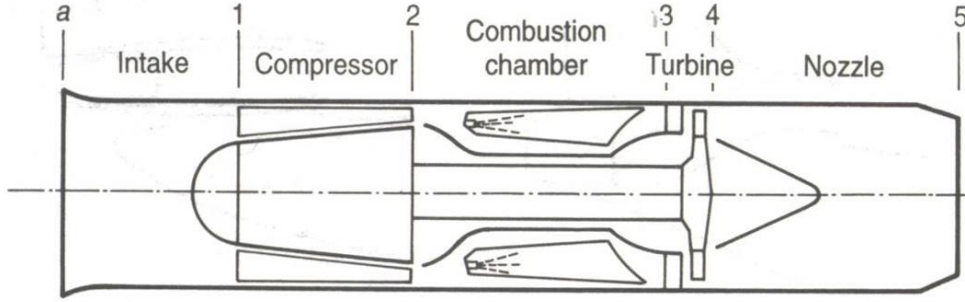


Figure 3. Schematic diagram of a turbojet [6].

Table 4. Summary of station numbers and their meanings for a turbojet engine.

Station	Description
a	Ambient
1	Compressor entry face
2	Compressor exit
3	Turbine entry
4	Turbine exit
5	Nozzle exit

Estimations were made for the efficiencies of the components to match the quoted static thrust values from JetCat. The dynamic performance was then characterised. The net thrust F_N developed by a turbojet is given by

$$F_N = \dot{m}_a(U_5 - U_a) + A_5(p_5 - p_a) . \quad (4)$$

where \dot{m}_a is the mass flowrate of air through the engine, U represents velocity, p the pressure, and A_5 the exit area. This is plotted in Figure 4 for the P400, which shows the thrust still decreasing with speed, but at a much slower rate than for propellers. This is due to the ram drag caused by the $\dot{m}_a U_a$ term in Equation (4), increasing as U_a increases [7]. The thrust then begins to reduce at a shallower gradient. The nozzle becomes choked as the ram pressure increases with airspeed until the nozzle pressure ratio (NPR) is greater than the critical pressure ratio. p_5 becomes the critical pressure, p_c , defined as

$$p_c = p_{04} \left[1 - \frac{1}{\eta_j} \left(\frac{\gamma_g - 1}{\gamma_g + 1} \right) \right]^{\frac{\gamma_g}{\gamma_g + 1}} , \quad (5)$$

where η_j is the nozzle isentropic efficiency, and γ_g is the ratio of specific heats for combustion gases. This is the pressure where the exit flow is sonic. The exit pressure is greater than the ambient pressure, giving an additional pressure thrust that counters the ram drag. This recovery of thrust at high speed gives the best dynamic performance, meaning that turbojets are the only system capable of reaching the design speed. They were therefore selected as the propulsion system of choice despite the number of contradictions shown in Table 2.

To meet the net-zero emission target, the engine shall be run on Synthetic Air Fuel (SAF) rather than Jet-A1. This is simpler to integrate than hydrogen, as it can be used in place of Jet-A1 with no modification.

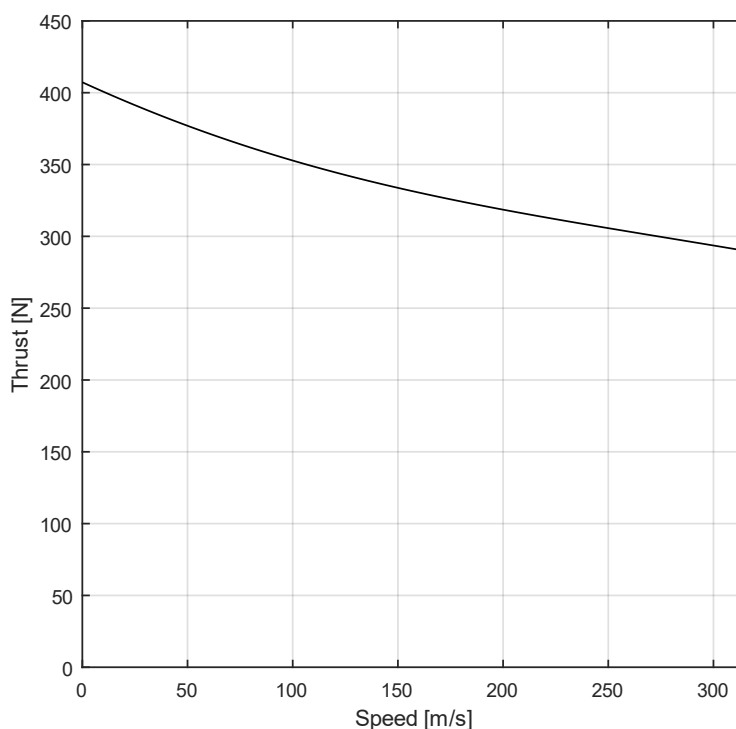


Figure 4. Thrust against speed for the JetCat P400-PRO.

1.3.1.3 Down-Selection of Airframe Layout and Peripherals

The airframe layout concepts were then generated, and an initial layout chosen (Figure 5), arriving at an ogival double-delta with twin vertical fins. Details of this can be found in the Aerodynamics and Stability & Control reports [5, 8]. The avionics and structures concepts were selected, and the initial performance calculations performed as [9-11] show.

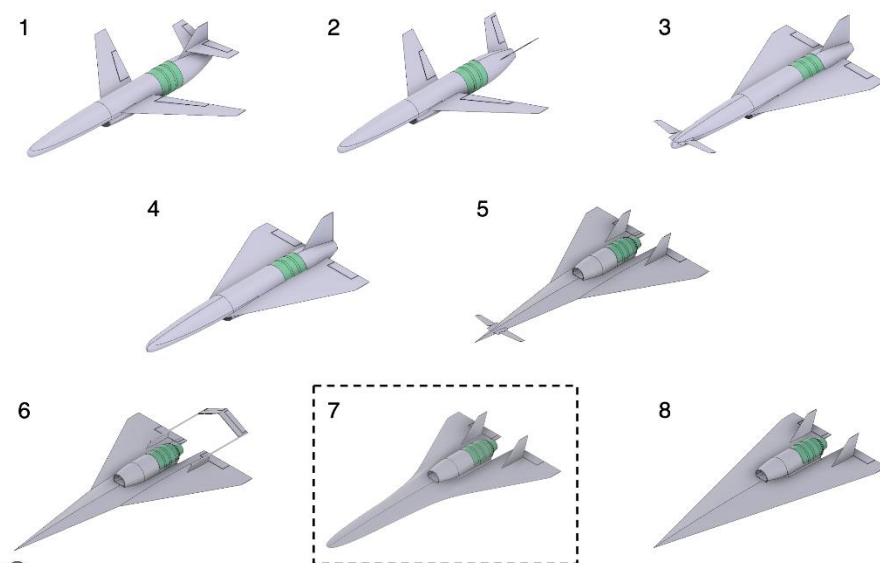


Figure 5. Layout concepts generated with the selected version boxed - featuring a double-delta and twin tail fins [1].

1.4 Engine Selection

Each of the turbojets available from JetCat and its competitor, Behotec, were modelled as the P400 was. It was assumed that the engine would account for approximately 30 % of the weight of the aircraft to estimate the drag from wing-loading [5]. This was done for level flight, and a 5g turn as prescribed by the performance engineer [9]. An example of the data generated is shown in Figure 6 for the P400. Note, the wing loading for analysis was chosen to be 300 g/dm³.

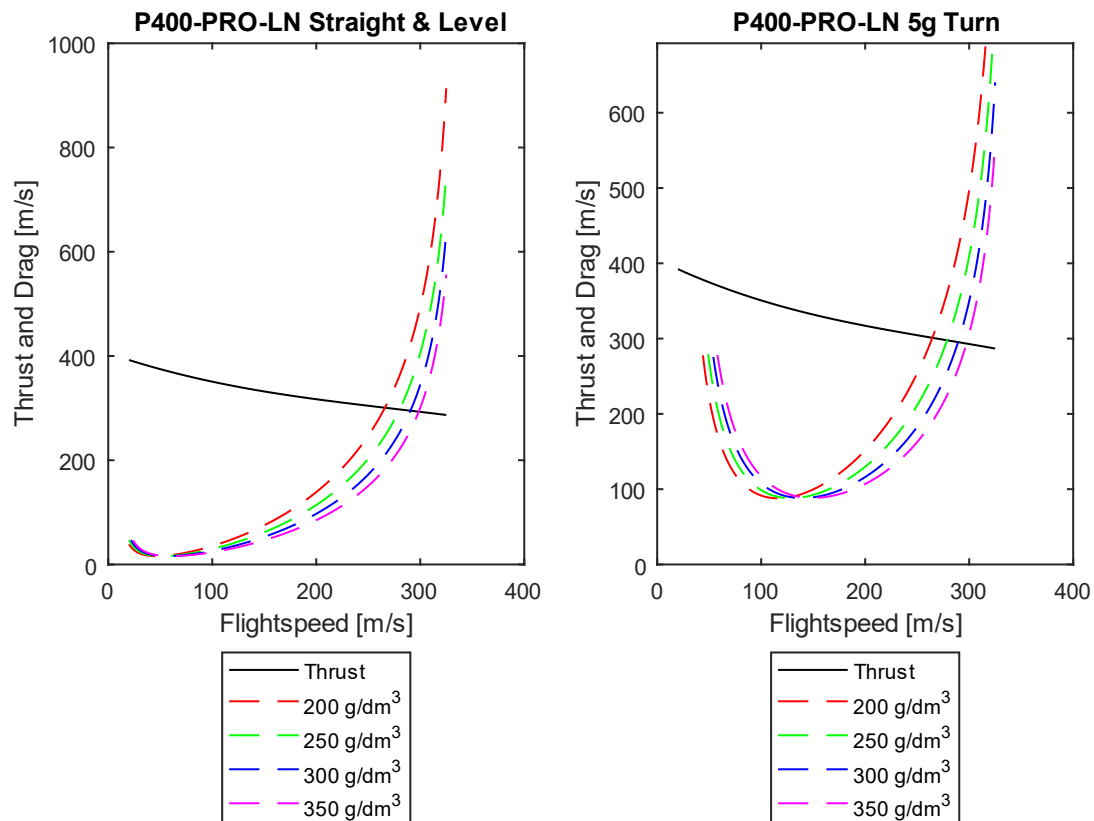


Figure 6. Thrust and drag at different wing loadings against speed for the JetCat P400. Dashed lines represent drag values.

The engines were compared on four performance parameters all evaluated at Mach 0.8 - the thrust-to-drag (F/D), thrust-to-area (F/A), thrust-to-weight (F/W) ratios, and cost. Each parameter was assigned a weighting based on its rank in importance. The engines were ranked from worst (1) to best (9) and the weighted sum was calculated (Table 5). Figures 7 and 8 show the weighted total and the individual weighted rank characteristics respectively. Overall performance peaks between 250-350 N of static thrust. Above this range, the cost increases disproportionately, alongside the size and weight leading to more drag. The 300-350 N class engines occupy a well-filled market maximising the likelihood of acquiring an engine. The JetCat P300 is the most available in the UK and so it was selected. Since the B350 will be identical in form factor to the P300 and B300, the engine could be upgraded in the future with minimal impact to achieve an even higher top speed.

Table 5. Decision matrix used to select the turbojet for the aircraft. Note that the model name denotes the static thrust. See Appendix A – Turbojet Decision Matrix, for the values for each engine.

Company	JetCat							Behotec		
Model	P220	P250	P300	P400	P500	P550	P1000	B300	B350*	Weighting
<i>F/D</i> rank	1	7	4	2	5	8	3	6	9	4
<i>F/A</i> rank	1	4	5	7	2	6	8	3	9	1
<i>F/W</i> rank	2	8	5	3	4	6	1	7	9	2
Cost rank	6	9	8	4	3	2	1	7	5	3
Weighted Total	27	75	55	33	39	56	25	62	78	10

*The Behotec B350 is unreleased and based on the same platform as the B300, in the same way the JetCat P500 and P550 are. Its performance and cost have been estimated using the same percentage change in parameters as between the JetCat P500 and P550.

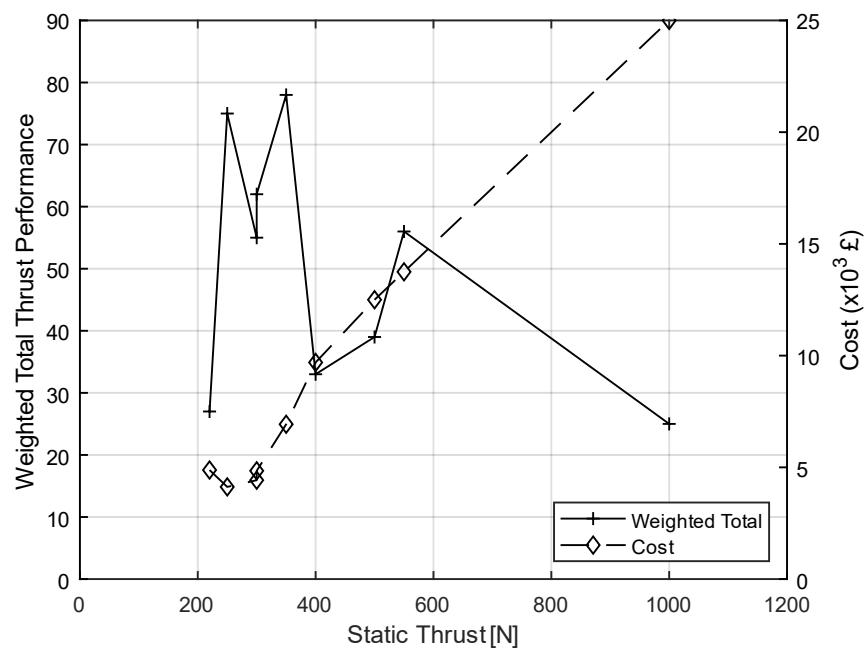


Figure 7. Weighted total thrust performance against static thrust for JetCat and Behotec engines.

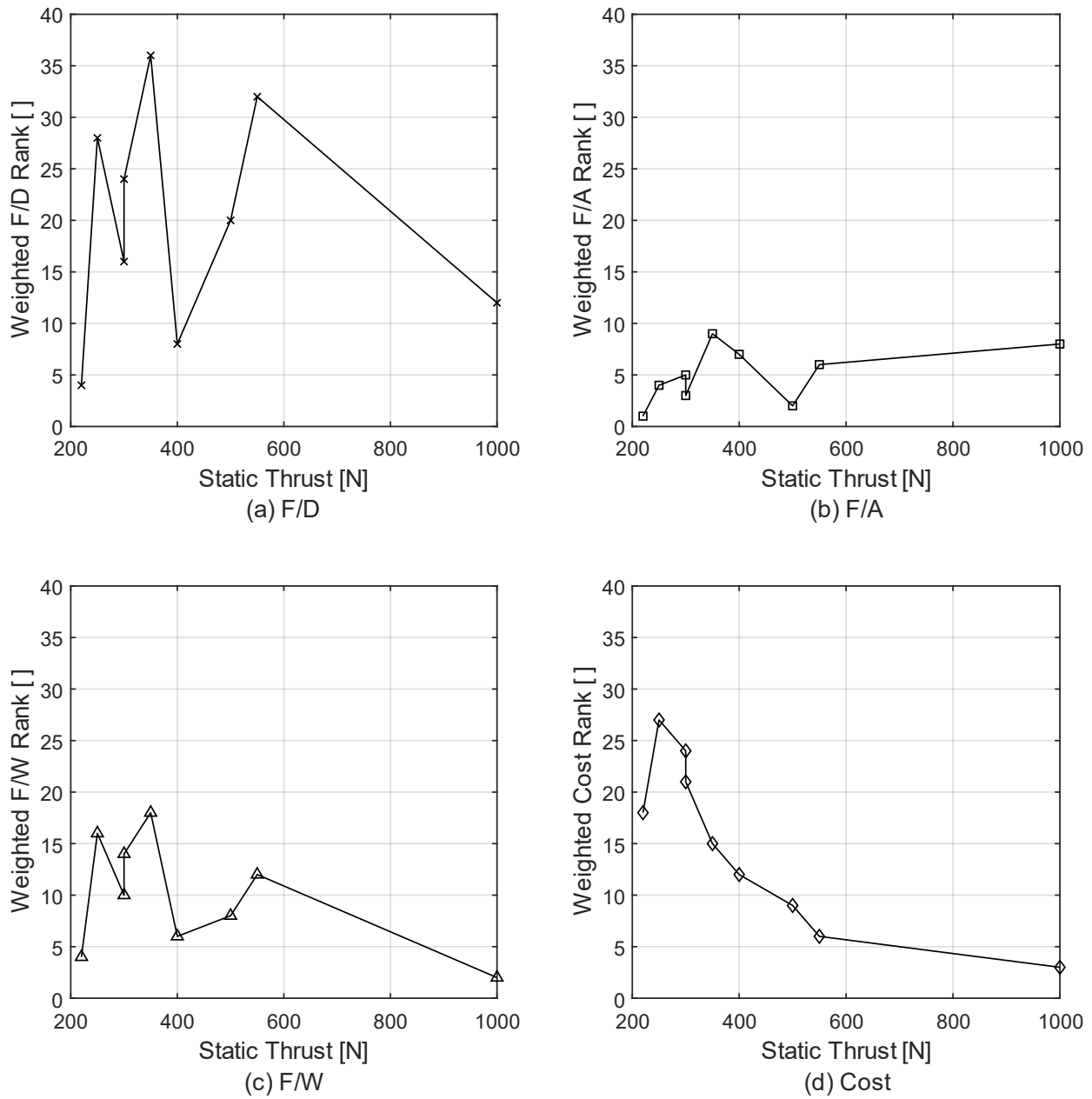


Figure 8. Weighted ranks for (a) Thrust-to-drag, (b) Thrust-to-area, (c) Thrust-to-weight, and (d) Cost against static thrust.

1.5 Inlet

1.5.1 Inlet Type

The P300 uses a centrifugal compressor, which can accept a maximum Mach number of 0.4. Since the aircraft is targeting a Mach number of 0.8, the flow must be decelerated efficiently by a diffusing inlet. Additionally, distortion at the compressor face (CF) must be minimised to prevent fatigue from cyclic loading. Dynamic stall of the blades can also occur resulting in surge although centrifugal compressors are more tolerant to this than axial ones [12].

A straight duct would be the simplest to design, but it would use up the entirety of the internal volume space needed for avionics and the fuel system, which makes it unviable. The engine could be raised off the centreline to free up the internal volume, but this would introduce an off-axis thrust component to the pitching moment which would lead to greater trim drag at top speed [13, 14].

The remaining options involve offsetting the inlet from the engine – these being twin side mounted inlets or a single s-duct. As Figure 9 shows, with aircraft angle-of-attack, side mounted inlets see significant local upwash making them susceptible to lip separation [15]. By contrast, fuselage and wing-shielded inlets see a more benign local incidence due to the physical blockage of the fuselage or wing [16], hence an s-duct was chosen.

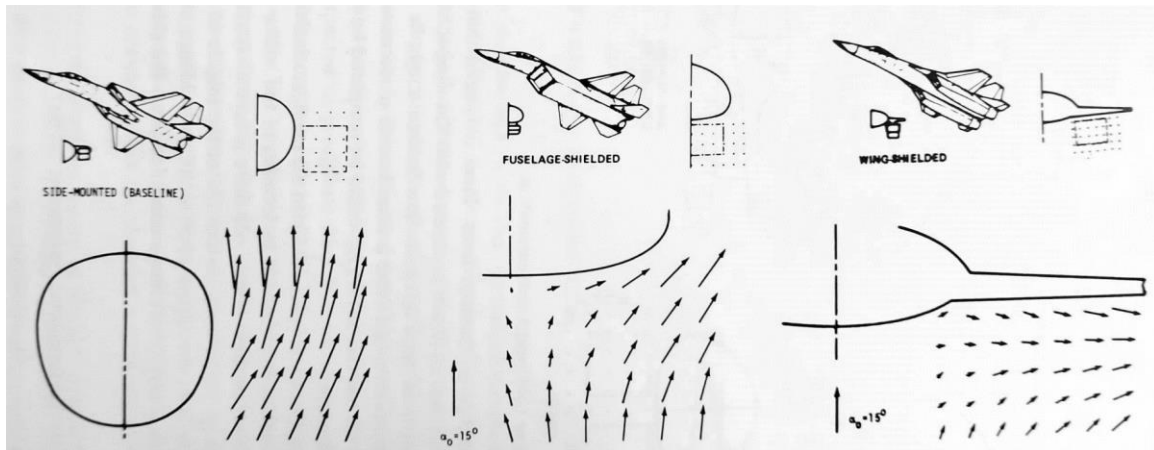


Figure 9. Comparison of vector flowfields for side mounted, fuselage-shielded, and wing-shielded at an incidence of 15° [16].

Mounting the inlet on the underside of the aircraft would make a belly landing infeasible, as this requires a smooth surface. A top-mounted inlet introduces aerodynamic complications. Namely, the inlet would be aft of the expansion on the suction surface of the aircraft; the additional backpressure may cause the boundary layer to separate and be ingested by the inlet. At high incidence, the wing root vortices would likely enter the inlet, introducing high swirl and distortion to the compressor [12, 16, 17]. To solve this, the aircraft would take off and perform the record attempt with the inlet and tailfins on the underside for optimum propulsive performance. At final approach, when the engine is switched off, it would be rolled 180° to land on the smooth belly. For further details, see the Performance report [9].

1.5.2 Inlet Sizing

The throat area, A_t , was determined targeting a throat Mach number (M_t) of 0.65 at the design speed, which gives reasonable performance over a range of flight conditions [16]. At high M_∞ , part of the diffusion is completed before the duct begins, reducing the boundary layer losses accumulated in the duct [18]. Using the isentropic relations, the total conditions in the freestream can be calculated. The static conditions at the throat are then calculable and the continuity equation can be used to give the throat area A_t [18], found to be 2100 mm².

The throat shape was chosen to be rectangular with fully semi-circular ends. This allowed the height of the inlet to be minimised to reduce the reflex in curvature on the external recovery of the inlet as Figure 10 shows. An aspect ratio of 3 was selected to minimise this reflex giving a height of 29 mm and an overall width of 87 mm. The semi-circular ends minimise the formation of secondary structures that are characteristic of the junctions of

a rectangular duct [2, 19]. It also separates the secondary structures formed on the inside surface of the s-duct reducing total pressure loss and distortion at the CF [18].

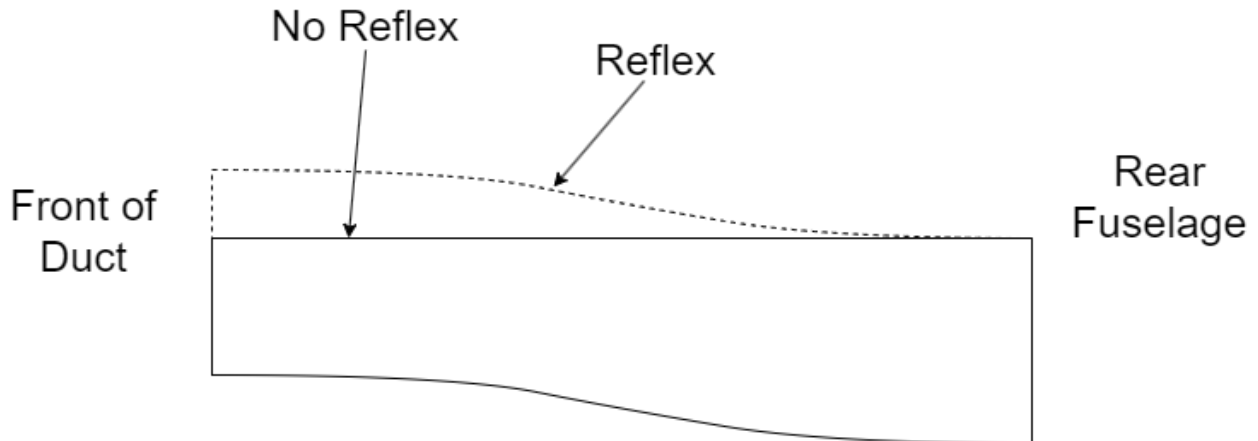


Figure 10. Sideview of s-duct showing external inlet profiles recovering to the rear fuselage.

A schematic of the key dimensions of the s-duct are shown in Figure 11. It is more convenient for measurements to be made at the Aerodynamic Interface Plane (AIP), shortly upstream of the CF. The offset was calculated as 51.8 mm to clear the fuselage and not ingest its boundary layer. The latter's thickness was calculated from turbulent flat plate correlations [20], with a safety factor of 1.5 applied [12]. An axial length-to-AIP diameter of 5 was determined to minimise total pressure loss and distortion as Papadopoulos et al. [18] discovered (Figure 12). The AIP diameter was larger than the compressor, at 87 mm, to fit around the starter motor struts. The diameter used for the axial length calculated was the CF effective diameter accounting for the starter motor.

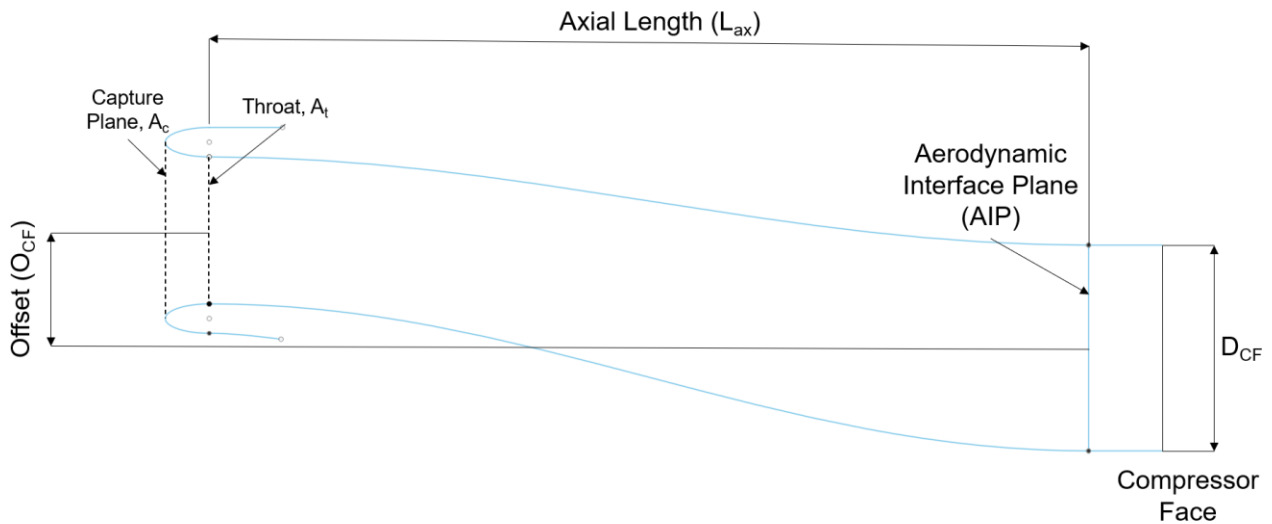


Figure 11. Schematic of the s-duct in sideview with the key dimensions labelled.

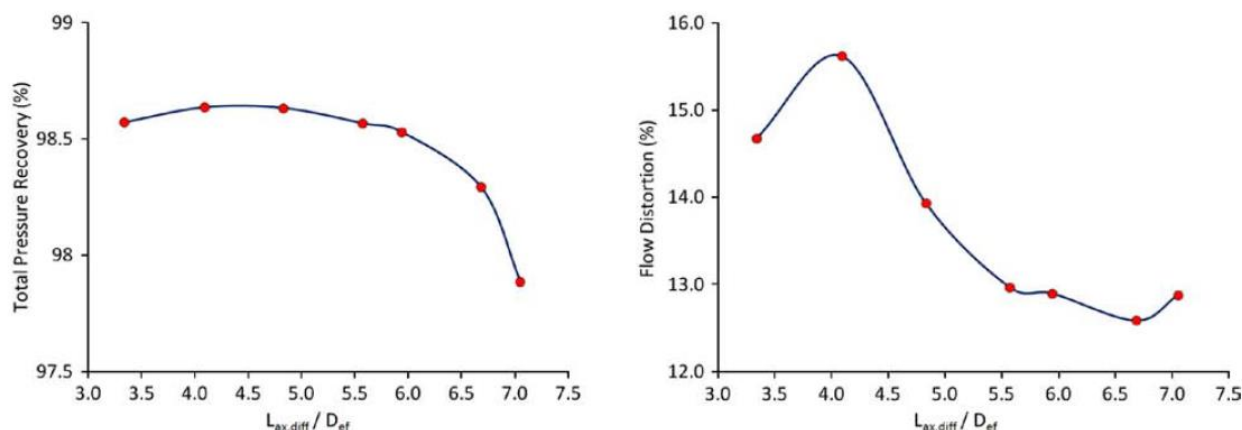


Figure 12. Total pressure recovery and flow distortion at the AIP against axial length-to-AIP diameter ratio [18].

The lip was designed such that the capture ratio (A_l/A_c), was 0.75, which gives adequate low-speed performance, and good high subsonic performance [16]. The lip profile is elliptical with an aspect ratio of 3 giving a height of 2.5 mm and a length of 7.5 mm. The key design parameters of the duct are summarised in Table 6.

Table 6. Key dimensions of the iteration 1 s-duct.

Dimension	Value
Outlet Area (mm ²)	5037
Throat Area, A_t (mm ²)	2100
Area Ratio ()	2.40
Throat Height (mm)	29
Throat Overall Width (mm)	87
AIP Diameter (mm)	87
Offset (mm)	51.8
Axial Length (mm)	324

1.6 Fuel System

The requirements of the fuel system are to:

- Store enough fuel such that the entire world record attempt can be completed – estimated at 0.53 litre [9].
- Ensure that no air bubbles are passed to the engine, which could lead to engine flame-out.
- Be filled and drained whilst in the aircraft.

To safely meet the fuel volume requirements, the fuel tank would need to fill the remaining volume closely giving a complex shape. With the time remaining until the Preliminary Design Review (PDR), developing the undocumented process of using a bag as Herbrich does was deemed too risky. Instead, a custom Kevlar fuel

tank was proposed. A mould would be routed out of foam with a Kevlar lay-up wrapped around it. Figure 13 shows the proposed shape in the aircraft. To ensure air is not ingested, the fuel line extends into the tank and has a lead weight so that it is always submerged.

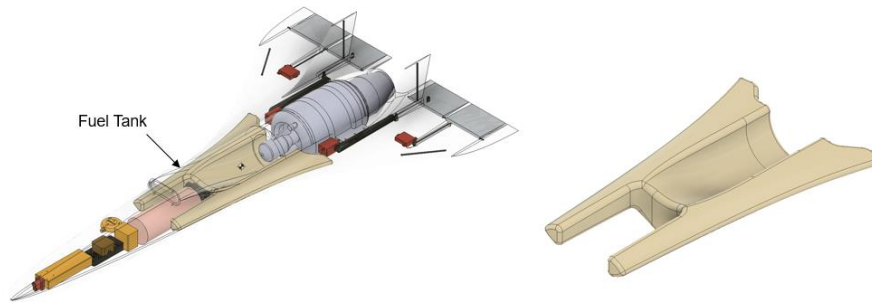


Figure 13. Kevlar fuel tank for the first iteration of the aircraft [1].

Discussions were held with sponsor, Callen-Lenz, who are consultants in the UAS field [21], and concerns were raised regarding the manufacturability of the tank. With large curvature changes and small radii, the tank was liable to leak. As the tank drains, it would fill with air. The sloshing caused by manoeuvres would aerate the fuel increasing the risk of air ingestion. The fuel tank occupying the entire remaining volume also meant a Universal Air Trap (UAT) could not be fitted to remove this air. Understanding and mitigating these problems formed the basis of the development plan for this subsystem.

1.7 Further Development Plan

The fuel system will be revisited aiming to mitigate against air ingestion more effectively. Ground systems and processes will also be developed to fuel and drain the aircraft on the ground.

The nozzle on the JetCat P300 is attached with a series of bolts, making it easily replaceable. The potential to optimise the nozzle for the design speed is to be investigated, considering whether a De Laval nozzle would give significant benefit.

Both academics and industrialists expressed concerns over the use of an s-duct due to the inability to characterise quantitatively the total pressure loss and distortion caused by the highly complex secondary flow features. To address this, use of CFD was planned to quantify the inlet performance and optimise its design.

PART II: DETAILED DESIGN

2.1 Fuel System Redesign

A soft bag was re-evaluated for the fuel tank as it would shrink around the remaining fluid rather than ingest air when it drained. One of the principal concerns was the complexity of the shape for a single bag to fill would require a custom tank. Therefore, it was elected to use two separate bags which could be simpler in shape. The maximum volume in each space is 0.86 litre, and so two 2 litre IV bags would be used to give sufficient flexibility when filled to conform to the available space. To further ensure that the possibility of air bubble ingestion is minimised, a UAT was added even though Herbrich's design does not use one. This was done to remove any air that remains in the tank after fuelling because of user inexperience. It also acts as an additional reservoir of fuel in addition to the tanks. Since two bags are used, the UAT must have two input lines. Therefore, the Digitech Air Trap 160 was selected as it is the smallest UAT available with this.

Figure 14 shows a schematic of the fuel system including the ground station. The two bags feed through the UAT to the engine via its integrated pump. The ground station contains an air pump that drains the tanks of air. An external reservoir is connected to the UAT via a pump with a filter between, which fills the tanks. Once filled, the external fuel pump is disconnected, but the reservoir is connected directly to the UAT. This means that when the engine is running through the start-up sequence, fuel is drained from the reservoir and not the tanks. The reservoir is then disconnected, and fuel is then drained from the tanks for the flight. After the flight, the external fuel pump is reconnected to drain the remaining fuel into the reservoir.

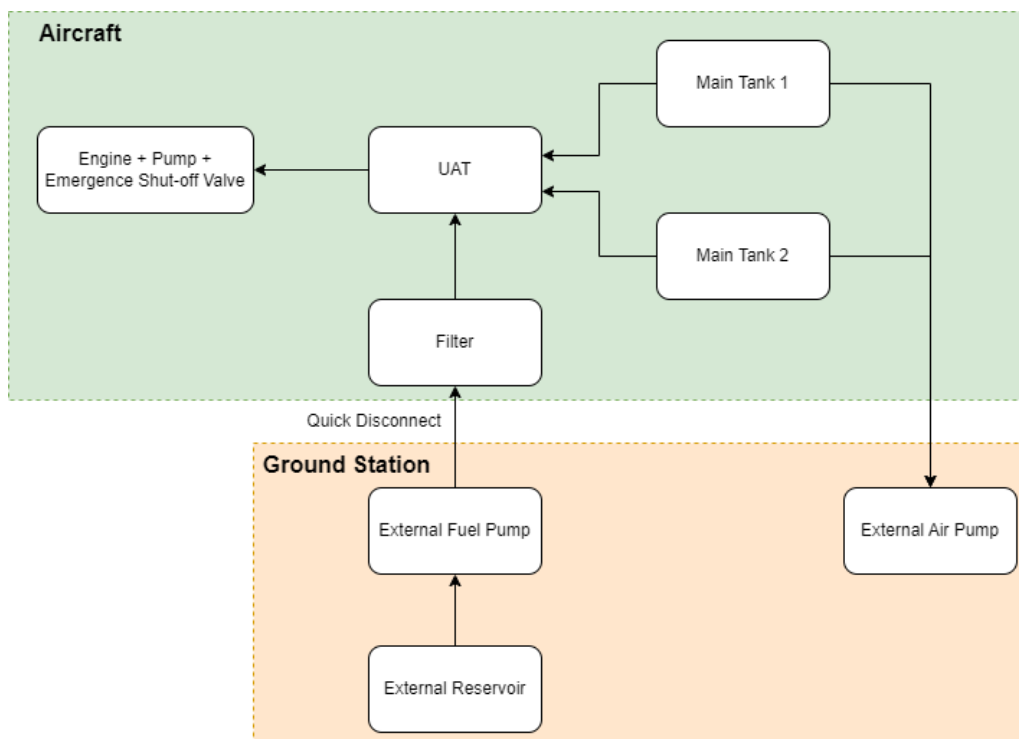


Figure 14. Schematic of the fuel system.

Concerns were raised over the possibility of the bag to fold in on itself as it drained, blocking the exit hole. To mitigate this, a rubber pipe was added that extends into the tank. This pipe is perforated along its length. This

ensures fuel is drained from the whole length of the pipe and if any holes are blocked, the remaining ones will allow fuel to continue to be taken.

2.2 Nozzle

The nozzle on the JetCat P300 is secured using a series of circumferentially spaced bolts. This means that it is easily removed and can be replaced by a custom nozzle, sized for optimal operation at Mach 0.8. First, the potential benefit of a De Laval nozzle was considered. However, these only give a meaningful increase in thrust above NPR greater than approximately 6 (Figure 15) [2]. The NPR at the design condition is only 2.74, and so the slightly greater thrust is not worth the extra size and weight.

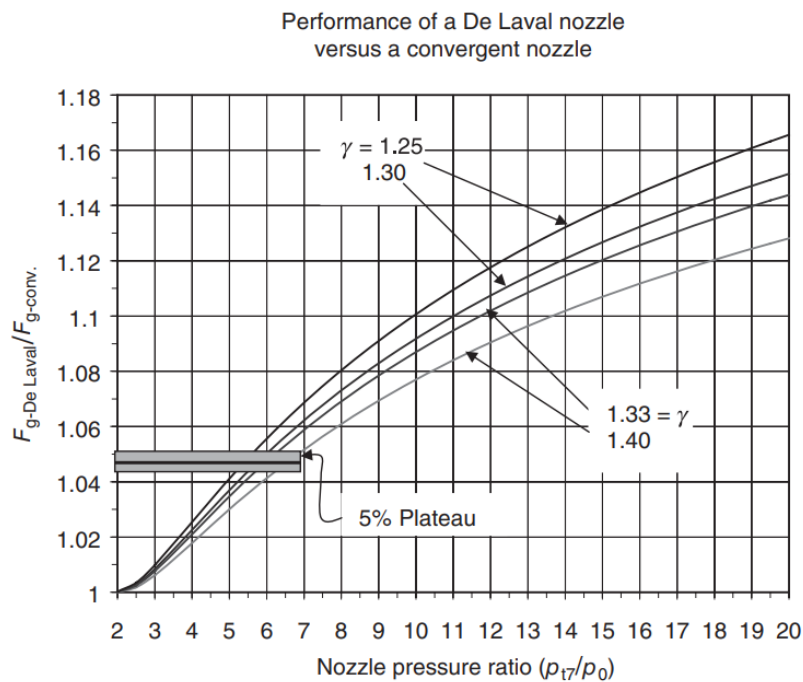


Figure 15. Ratio of gross thrust of a De Laval nozzle to a converging nozzle against NPR. N.B. $\gamma = 1.333$ was the value used for analysis purposes [2].

The optimum exit area for the nozzle was found by solving for the exit density with the ideal gas law having acquired the exit pressure and temperature from the marching analysis [6]. The continuity equation was then solved for the ideal A_5 , which was found to be 1655 mm², giving a diameter of 45.9 mm. Similar analysis was performed for the stationary case, and it was found that the true diameter of the stock nozzle was 15 % higher than this, which has a diameter of 63.5 mm compared to the analytical value of 54.0 mm. This was attributed to the stock nozzle accounting for boundary layer growth. This was adopted to give a nozzle diameter of 52 mm. A length-diameter ratio of two was used, giving a length of 105 mm, to allow mixing of the high swirl turbine exit flow to become uniform at the exit [22].

There was insufficient time to perform a thermal analysis on the nozzle to find the optimum material for mass, and so it was decided to keep the stock nozzle. In future work, the thermal effects will be investigated, and a new nozzle fitted. Time was instead invested on setting up the inlet CFD model.

2.3 Inlet CFD Analysis

2.3.1 Computational Model

A computational model of the inlet was made using Simcenter STAR-CCM+, a finite volume method commercial CFD package, to quantify and reduce the total pressure loss, and the distortion at the AIP. The domain is shown in Figure 16.

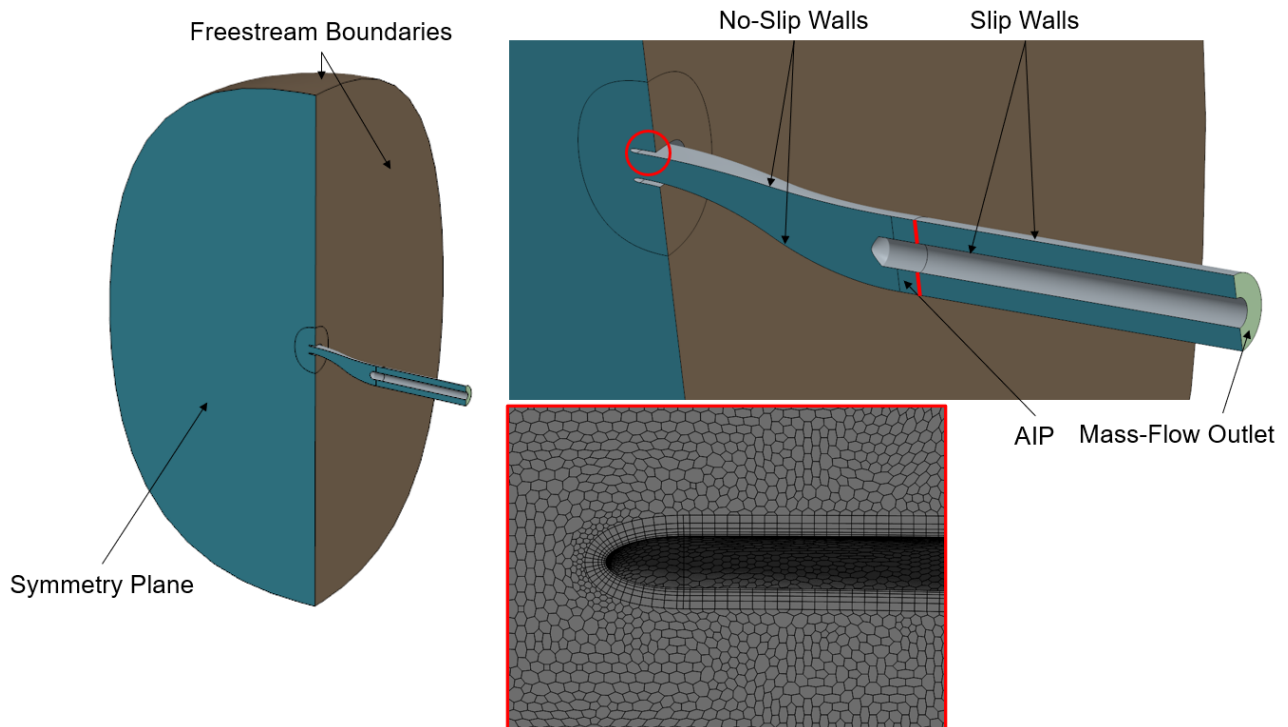


Figure 16. CFD flow domain and mesh structure inside the main duct.

Only half the inlet was considered allowing for a reduced cell count with a symmetry boundary employed at the symmetrical plane. The domain inlet and outlets downstream of the lip were freestream boundaries prescribing the Mach number of 0.8. The wing-body-nacelle was not modelled as primary interest was in the internal duct and lip flow. The AIP was defined 30 mm in front of the compressor face, just as the starter motor diameter reduces as Figure 17 shows.

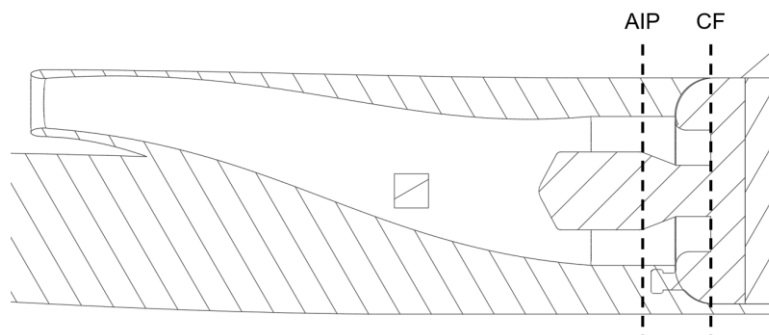


Figure 17. Sideview schematic section of the s-duct showing the AIP and CF.

The no-slip condition is applied to the walls with a blended wall function until the AIP. This function blends between the logarithmic region of the boundary layer ($y^+ > 30$), where y^+ is the non-dimensional normal wall distance, and the linear region in the viscous sublayer ($y^+ < 5$), according to the universal law of the wall [23], similar to the function of Spalding [24]. Downstream of the AIP, the duct is extended by five diameters with a mass-flow outlet at the end as was performed by SAAB in [25] (Figure 18). The mass-flow outlet tends to enforce a uniform velocity field, so the distance minimises its impact at the AIP.

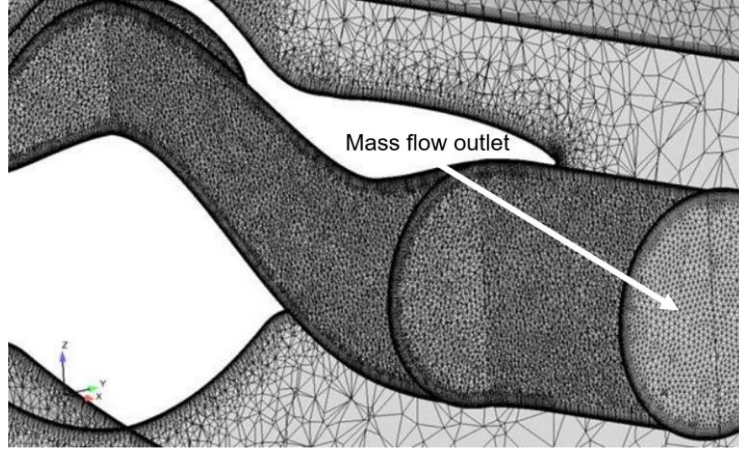


Figure 18. SAAB unstructured mesh with a virtual extension of the duct past the AIP to a mass-flow outlet [25].

The domain was discretised using a polyhedral unstructured mesh, with inflation (prism) layers used at walls to capture the boundary layer. An unstructured mesh was employed following the example of Delot et al. [25], and the complexity of geometry and timeframe available meant developing a structured mesh was not feasible. The unstructured approach allows the mesh to be refined where it is needed locally without wasting storage [26]. Polyhedrons were used as each cell has many neighbours and so gradients are well approximated, they are less sensitive to stretching than tetrahedrons, and numerical diffusion is reduced as mass is exchanged over more faces [27].

To accurately capture the steep velocity gradients in the boundary layer (Figure 19), the first cell centroid height, y_{c1} , should have a y^+ of less than one so that the smallest turbulence length scale is captured [28]. The total height of the inflation layers should capture the maximum height of the boundary layer, y_{BL} , and it is good practice to have a cell-height growth rate of approximately 1.2 [25]. To satisfy this, N layers are needed such that

$$y_{BL} = y_{c1} \cdot 1.2^{N-1}, \quad (6)$$

which yields

$$N = 1 + \frac{\ln \frac{y_{BL}}{y_{c1}}}{\ln 1.2}. \quad (7)$$

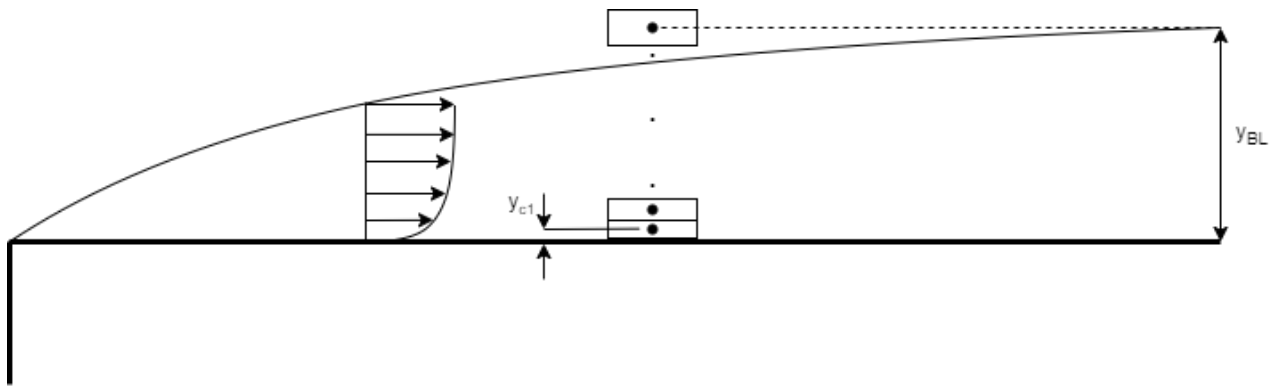


Figure 19. Inflation layers in a generic CFD domain.

Neither y_{BL} nor y_{c1} can be known in advance. An estimation was made for y_{BL} based on the author's previous experience of aerodynamic duct design, and a value of 5 was chosen for N based on settings in the available Siemens training materials.

The Reynolds Averaged Navier-Stokes (RANS) equations were solved, noting that unsteady techniques were not feasible due to limitations in computing power. The $k-\omega$ SST (Shear Stress Transport) model was used for turbulence closure. This provides greater accuracy in adverse pressure gradients and high curvatures in near wall-flow than the $k-\epsilon$ model. It blends to $k-\epsilon$ in the freestream since the standard $k-\omega$ model is sensitive to the freestream condition of ω [28]. Convergence was assessed based on the stabilisation of momentum and mass flowrate residuals and them being less than 10^{-4} [29].

Grid independence was ensured by refining the grid until the average Mach Number at the AIP, averaged over the final 200 iterations, was constant to a tolerance of ± 0.001 . Table 7 shows that Grid 1 is sufficiently converged. However, Grid 2 was used as this gave a less oscillatory value of average Mach number (Figure 20).

Table 7. Grid independence study.

Grid Level	Number of Cells	y^+_{min}	y^+_{max}	AIP Average Mach Number
1	552190	6.58	74.6	0.172
2	758746	5.26	59.7	0.171

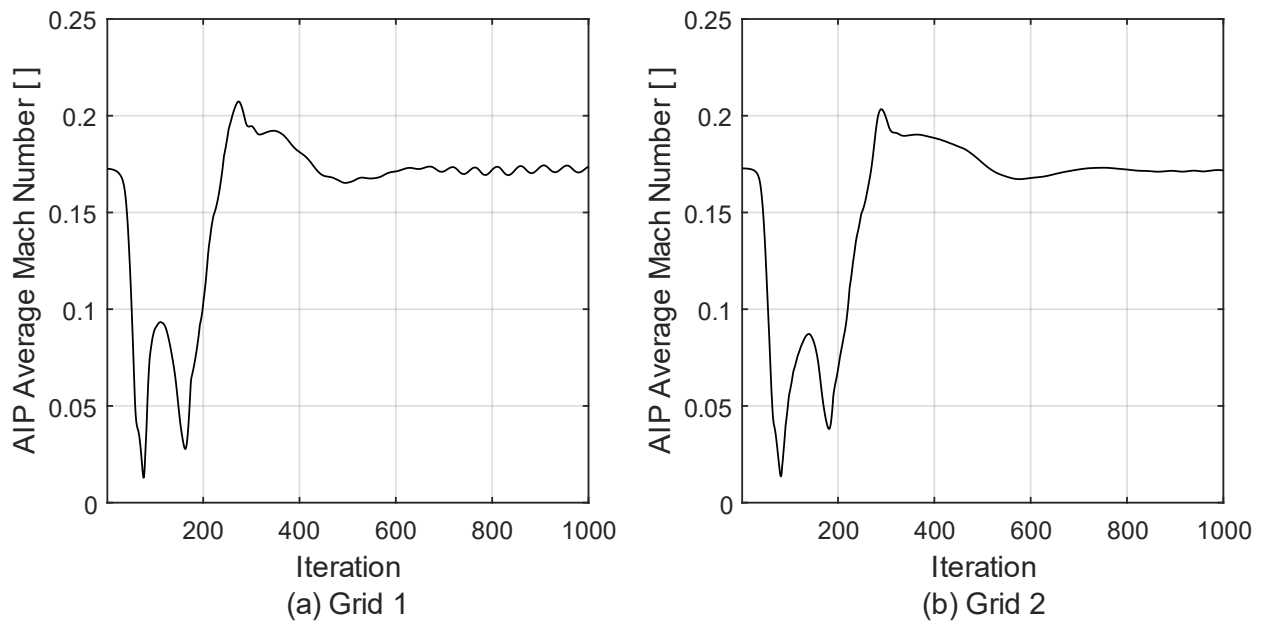


Figure 20. AIP Average Mach number against iteration for (a) Grid 1 and (b) Grid 2.

2.3.2 Limitations and Errors in the Computational Model

The computational model was set up and analysis performed over a three-week period. In addition, simulations were conducted on a PC. With these limits, sacrifices to the model accuracy had to be made.

The flow structures in s-ducts are highly transient in nature as shown by MacManus et al. [30], meaning the steady-state techniques used oversimplify the problem. Unsteady RANS (URANS) requires approximately twice the number of iterations to converge adequately [31], and with the time available, this was deemed too costly.

Ideally, a pressure outlet would be used at the duct exit, as in [18] and [30], rather than a mass flow outlet. However, this required knowledge of the static pressure at the compressor face. An alternative solution would be to create a converging-diverging nozzle at the end of the diffuser as ONERA did in [25] where the outlet is in the supersonic region having no effect on the AIP.

From Table 7, the y^+ values in the duct are all above one, meaning that the wall function is being used on the whole duct. Their use is highly questionable in separated flows [28], which are present in a diffusing s-duct as they are based off empirical flat-plate relations without any pressure gradients. Due to memory limitations, the grid could not be refined further to solve this, and so analysis continued knowing that the prediction of separation and wall-shear stress would be inaccurate. Given the limited data found on s-duct design, this will serve as a starting point for future work.

It was initially intended for the aircraft's forebody to be incorporated into the computational model and investigate the performance at low speed. This would allow for the verification that the inlet was not ingesting forebody boundary layer and show the effect of the fuselage shielding at the take-off condition, where lip separation is liable [12, 16]. It was then discovered that the PC would not be capable of running such simulations. If this had been known earlier, the domain would have been reduced to include only the internal surface using the standard $k-\omega$ model as it is appropriate for purely internal flows [32]. This would allow for the appropriate use of inflation layers to give a more accurate solution.

2.3.3 Results and Updates to the Inlet Geometry

A large separation was found on the inside surface of the Iteration 1 duct. This low energy flow then forms the onset to the upper half of the AIP as Figure 21 shows, giving an average total pressure ratio of 0.980. 100 mm upstream of the AIP, the characteristic wake-like vortical structures of an s-duct can be seen (Figure 22), indicating the model is capturing the main flow features expected. An external shock is predicted implying that the thickness of the lip is too large [12, 16].

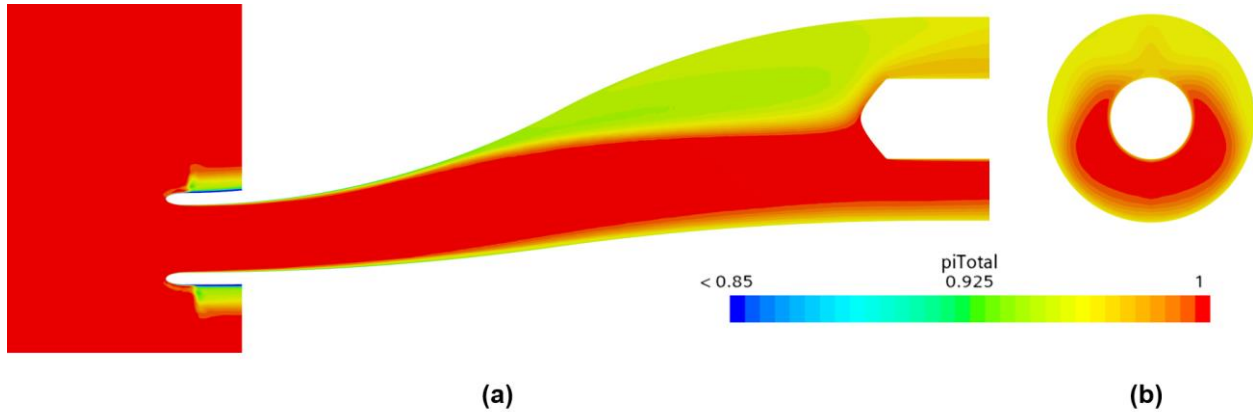


Figure 21. Total pressure ratio for iteration 1 inlet. (a) sideview of the centre plane. (b) front view of the AIP.

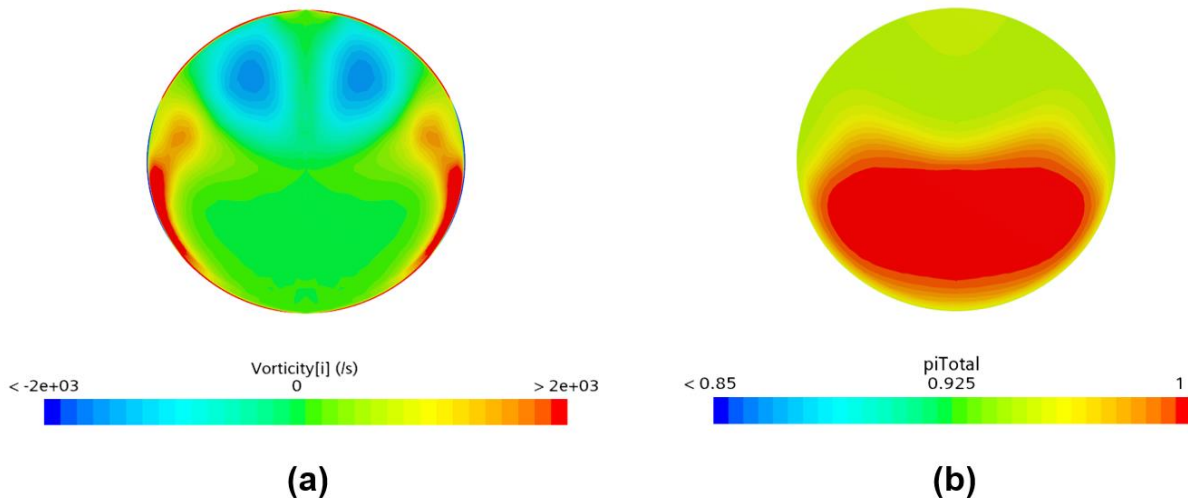


Figure 22. Iteration 1 streamwise vorticity (a), and total pressure ratio (b) at a plane 100 mm upstream of the AIP.

The separation was caused by the increased diffusion being conducted to avoid the starter motor struts leading to a greater adverse pressure gradient. The exit diameter was therefore reduced from 87 mm to 76.7 mm such that the annulus between the duct and starter motor had an area equal to the CF, taking the area ratio from 2.40 to 1.77. The more favourable pressure gradient reduced the separation to a minimal size (Figure 23). Figure 24 shows that due to the reduced separation, the vorticity previously present is now negligible. There is vorticity of the opposite sense, caused by the migration of the boundary layer towards the inside surface. The removal of the separation's blockage above the starter motor leads to a recirculating region in the new duct. This mitigates some of the benefit in total pressure ratio, but it is still increased from 0.980 to 0.987.

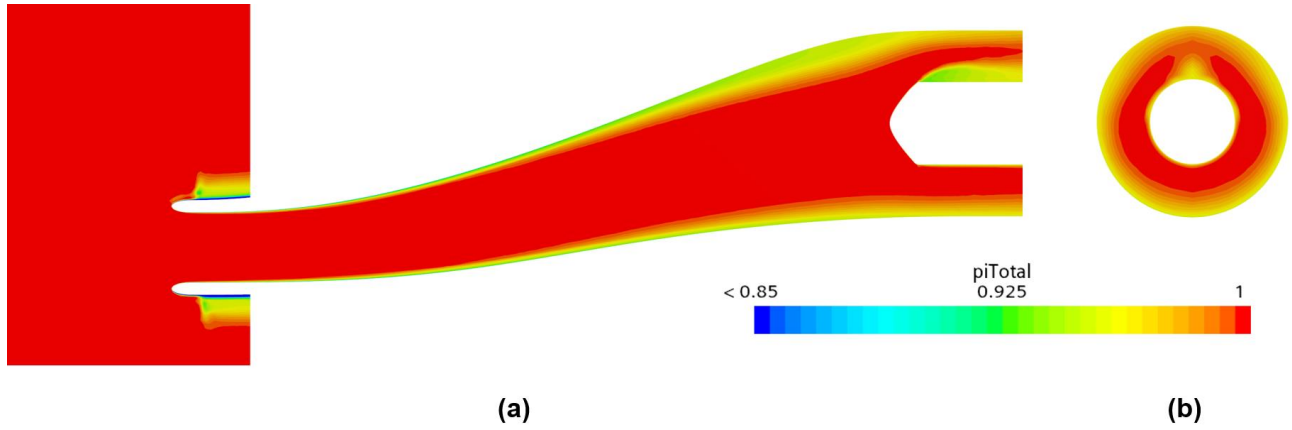


Figure 23. Total pressure ratio for iteration 2 inlet. (a) sideview of the centre plane. (b) front view of the AIP.

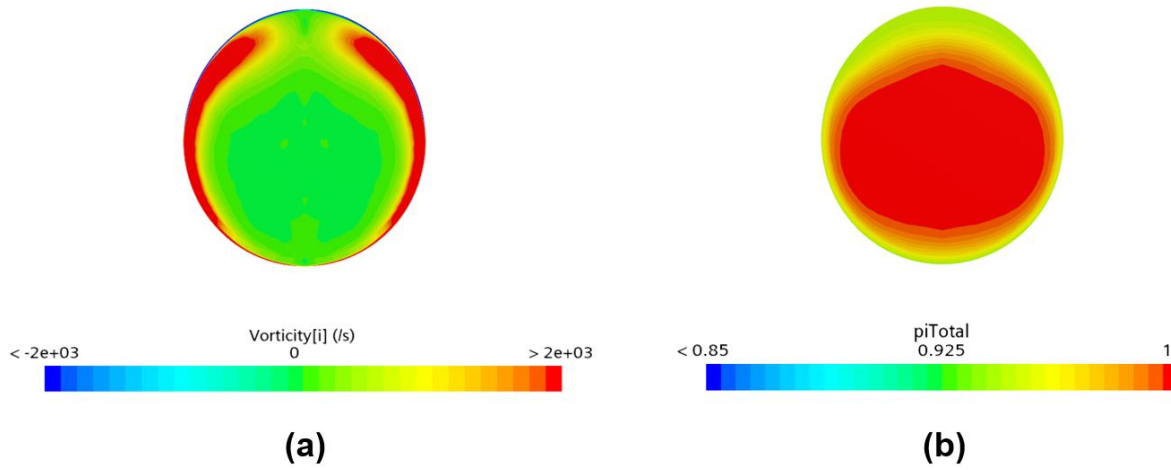


Figure 24. Iteration 2 streamwise vorticity (a), and total pressure ratio (b) at a plane 100 mm upstream of the AIP.

2.3.4 Quantification of Distortion [30, 33]

In rig tests, distortion is typically measured using rakes which contain concentric rings, each with 8 equally spaced probes to measure total pressure as Figure 25 shows. Distortion at the i^{th} ring can be measured by the radial total pressure distortion, $(\Delta P_R/P)_i$, given by the average total pressures on the AIP surface ($\overline{p_{0,AIP}}$), and along the ring ($\overline{p_{0,i}}$) through

$$(\Delta P_R/P)_i = \frac{\overline{p_{0,AIP}} - \overline{p_{0,i}}}{\overline{p_{0,AIP}}}. \quad (8)$$

The radial distortion index (RDI) is the maximum value, while the average radial distortion is the mean. For each ring, the extent parameter, θ_i^- is the total angular displacement where $p_0 < \overline{p_{0,i}}$. It indicates the time spent by a compressor blade in low total pressure zones.

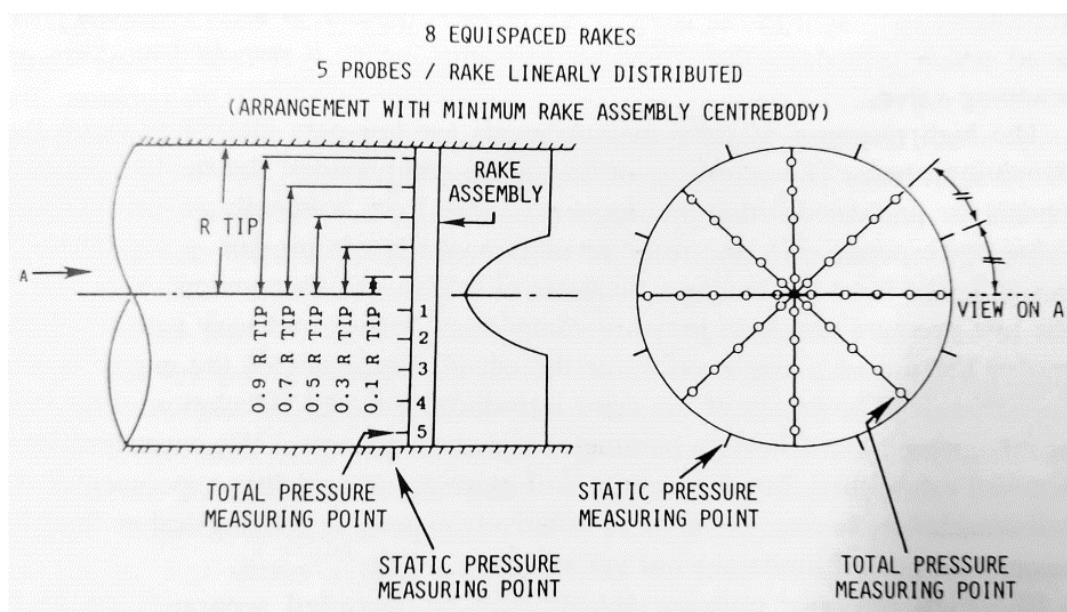


Figure 25. Instrumentation for measuring distortion [16].

Four equally spaced radial positions were used to monitor the distortion at the AIP as Figure 26 and Table 8 show. For each ring, the total pressure was plotted against angular position, θ , and the average computed using the trapezium rule for both iterations in Figure 27.

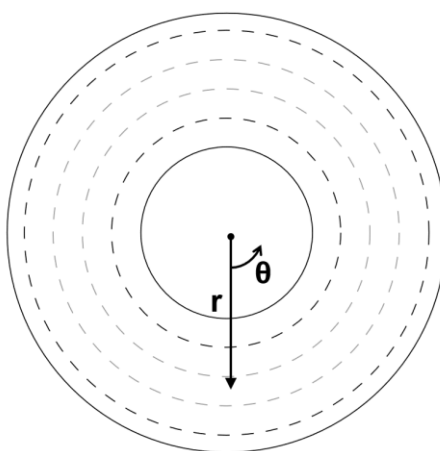


Figure 26. Schematic of positions for monitoring distortion at the AIP. Dashed lines are the measurement locations, and solid lines are the physical duct and engine starter walls.

Table 8. Summary of the radial positions to monitor distortion.

i	Non-Dimensional Radius, r/R ()	Iteration 1 Radius (mm)	Iteration 2 Radius (mm)
1	0.522	22.7	20.0
2	0.655	28.5	25.1
3	0.788	34.3	30.2
4	0.922	40.1	35.4

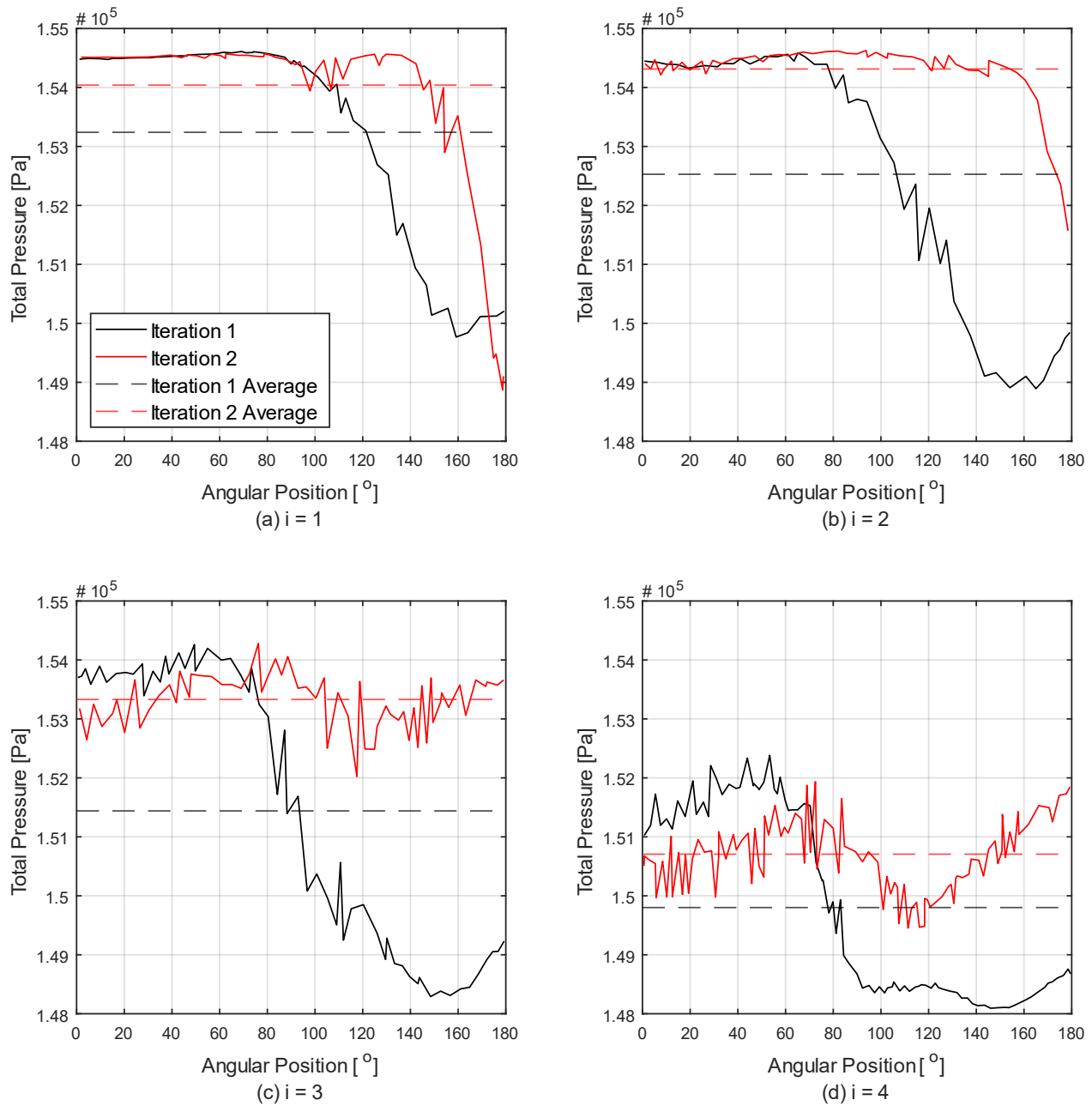


Figure 27. Total pressure against angular position for each ring plotted for both iteration 1 and iteration 2. The average value for each ring is also shown.

The second iteration duct has a more uniform total pressure distribution at all radii, lying closer to the average values. Equation (8) was used to calculate the radial total pressure distortion for each ring, and θ^- was also calculated. These were then plotted against r/R in Figure 28, which shows the maximum and average values have both decreased with the new duct. Table 9 summarises the decrease in distortion. This will mean the engine will experience less vibration and be less susceptible to surge.

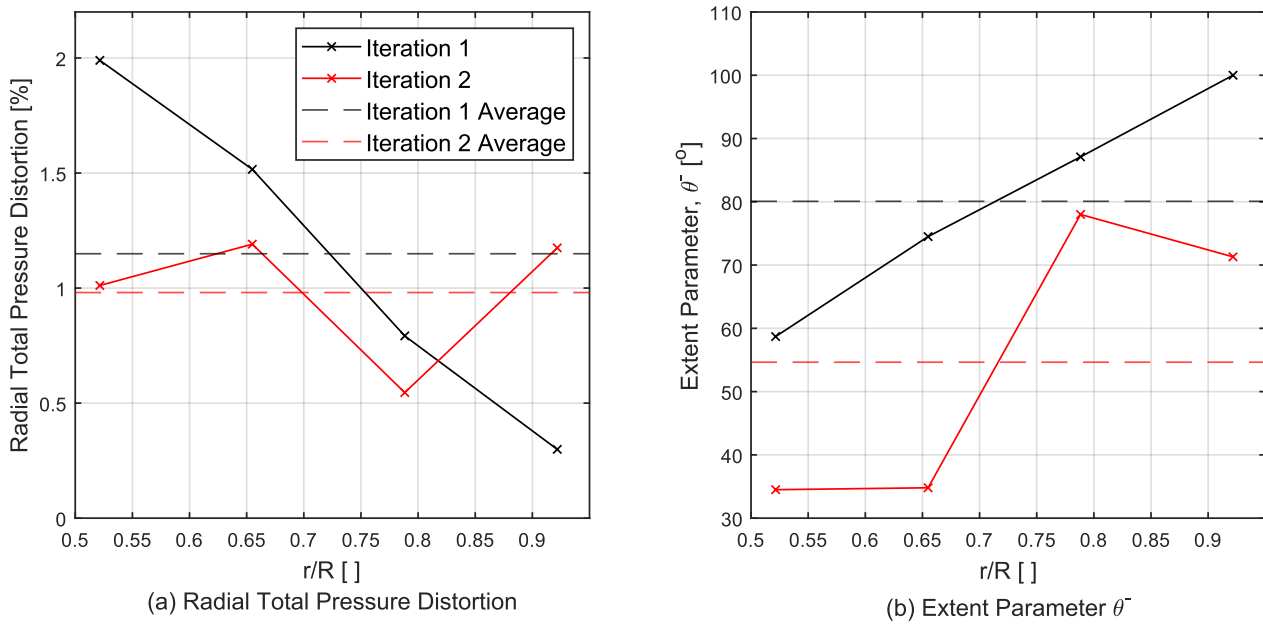


Figure 28. Radial total pressure distortion (a) and distortion extent parameter (b) against non-dimensional radius.

Table 9. Distortion metrics for Iteration 1 and Iteration 2.

	Iteration 1	Iteration 2	% Change (%)
RDI (%)	1.99	1.19	-40.2
Mean Radial Total Pressure Distortion (%)	1.15	0.981	-14.7
Maximum Extent Parameter (°)	100	78.0	-22.0
Mean Extent Parameter (°)	80.1	54.7	-31.7

While the presented work has shown an improvement in both average total pressure recovery and distortion, the P300's tolerance to this will only be known through experimental testing. To assess this, analysis of the engine's response to distortion is needed, in addition to improving and validating the computational model (Section 2.3.2) with experimental data. The inlet is upgradeable, as it will be additively manufactured [10]. Therefore, updated designs can be implemented rapidly.

2.4 Future Work

This report has laid the foundations for the preliminary design of the propulsion system. To progress into the detailed design and maximise the chances of success, key questions must be answered:

2.4.1 Validation of the Thrust Models

The thrust models were calibrated based on the static thrust values quoted by the manufacturer. No data is available for the dynamic performance of the engines, which would validate the model. This data could be collected from rig tests on an example engine using forced induction to simulate the ram pressure rise. This

data could then be compared to the outputs of the thrust model. If they agree, the model can be deemed accurate; if they do not, the models require refinement.

2.4.2 Fuel System Ground Testing

The fuel system has been designed based off industrial experience from Callen-Lenz. The most accurate way to verify that it supplies fuel without air bubbles would be to create a ground test rig. A test plan would include:

1. Orientation drain tests without an engine
 - a. Connect the fuel system to an external pump and drain it to a reservoir at multiple angles.
 - b. Monitor the build up of air in the UAT with fuel level.
2. Engine *in situ* tests
 - a. Connect the rig to the engine and perform the same test as above.
 - b. Monitor the engine thrust performance for each orientation with fuel level.

These tests would test the fuel system in a controlled environment without risking loss of an entire aircraft.

2.4.3 Alternative Fuels

The present solution uses SAF to reach the aim of net-zero flight emissions. Future work could look to develop the necessary systems to run the engine using hydrogen. This would eliminate flight CO₂ emissions and align with current research projects being conducted at the university.

2.4.4 Thermal Modelling

A thermal model would allow for a material to be chosen such that the nozzle does not soften and expand excessively. An initial 1-D model should be created, and this could be used to verify a 3-D finite element model to select an appropriate material and thickness aiming for minimum weight.

This modelling should also be performed on the structure around the engine itself. Rig tests on the engine would allow for the quantification of the boundary conditions for such a model. The required mass flow of air could then be calculated, and the inlet designed to bypass the required flow for cooling.

2.4.5 Inlet Testing and Improved Modelling

Section 2.3.2 details the shortcomings of the computational model and suggests improvements. The domain should be reduced to include the internal duct only to capture the internal flow structures more accurately. This would also allow for the contribution of drag from the internal surfaces to be quantified.

The lip geometry requires further investigation to eliminate the shocks which will contribute to aircraft drag. Other flight conditions such as take-off and off-design should also be considered to ensure the inlet does not stall in gusts and low-speed conditions.

If access to High Performance Computing (HPC) is available, the improved RANS results could be used to conduct Unsteady RANS (URANS) simulations. This would allow for the transient behaviour of the s-duct structures to be understood. Different duct area distribution strategies, such as Gerlach area shaping [34], could also be tested. Adjoint shape optimisation could be employed to assess surface sensitivity at different positions in the duct with a goal function of increased total pressure and reduced distortion at the CF[35].

The engine tolerance to distortion has not been assessed. Without knowledge of the surge margin, it cannot be known whether the engine will be able to operate with the onset given. Rig tests should be performed to determine the engine's distortion tolerance to de-risk this. Only total pressure distortion has been considered, and so analysis of the duct's swirl distortion and the engine's resistance to this should be evaluated.

2.5 Conclusion

To break the current world record, turbojets are the only viable propulsion type with the dynamic thrust necessary to overcome the drag at high subsonic speeds. It was found that turbojets reach a peak in thrust relative to their size, weight, and cost at the 250-350 N range. Therefore, the JetCat P300 was chosen running on Synthetic Air Fuel to achieve net-zero flight emissions. Given the volume constraints of RC aircraft, a pair of flexible bags are necessary to conform to the complex internal shape. This also means that for an inlet to be fitted, it must be offset from the centreline. The inlet area for the diffuser was determined as 2100 mm² to best performance at Mach 0.8. The offset introduces secondary structures which can inhibit engine performance. A computational model was developed to characterise the distortion of the inlet. This then informed modifications to its design, reducing the exit diameter, and making the surfaces curvature continuous, which improved the total pressure recovery from 0.980 to 0.987, and the Radial Distortion Index from 1.99 to 1.19 %. The analysis performed can now be built on in future work over Final Year Projects (FYP) in the coming year.

2.6 Project Overview

The propulsion system formed a central part of the project requiring collaboration with aerodynamics and performance to generate performance models and to generate the concept of flying upside down. Due to the highly compact design, integration constraints had a large effect, leading to the necessity for an s-duct introducing significant risk. The use of CFD to model this, while still requiring refinement, has developed the parameters by which to measure inlet performance. With the timeframe and hardware available, analysing both internal and external properties of the inlet led to a reduced quality in results for the internal flows, and not enough time to analyse the external flows. If this project were to be repeated, there would be a focus on the internal aerodynamics solely.

The preliminary design presented, technical drawings of which can be found in Appendices B-D, has generated a further set of more specific research questions which can be answered over the course of a series of FYPs. This more detailed work will further develop parts such as the s-duct and the fuel system, increasing the likelihood of the success of The Mach Initiative breaking the world record.

2.7 References

- [1] D. Sykes, "The Mach Initiative: Project Manager's Report with a Technical Integrator's Perspective," University of Bath, Bath, 2023.
- [2] S. Farokhi, *Aircraft propulsion*, Second edition. ed. Chichester, England: Wiley, 2014.
- [3] P. M. Sforza, *Theory of Aerospace Propulsion*. Oxford: Elsevier Science & Technology, 2011.
- [4] J. M. Seddon, *Basic helicopter aerodynamics*, 3rd ed. Chichester, England Hoboken, N.J.: Wiley, 2011.
- [5] M. Jones, "The Mach Initiative: Aerodynamics Report," University of Bath, Bath, 2023.
- [6] H. I. H. Saravanamuttoo, *Gas turbine theory*, 5th ed. Harlow: Financial Times Prentice Hall, 2001.
- [7] N. Cumpsty, *Jet Propulsion : A Simple Guide to the Aerodynamic and Thermodynamic Design and Performance of Jet Engines*, 2nd edition. ed. Cambridge: Cambridge University Press, 2003.
- [8] T. Li, "The Mach Initiative: Aircraft Stability and Control," University of Bath, Bath, 2023.
- [9] T. Gilmour, "The Mach Initiative: Performance Report," University of Bath, Bath, 2023.
- [10] G. King, "The Mach Initiative: Structural Analysis and Design," University of Bath, Bath, 2023.
- [11] J. Martin, "The Mach Initiative: Avionics Design," University of Bath, Bath, 2023.
- [12] J. Seddon, *Intake aerodynamics : an account of the mechanics of flow in and around the air intakes of turbine-engined and ramjet aircraft and missiles*. London: Collins, 1985.
- [13] M. J. Abzug, *Airplane stability and control : a history of the technologies that made aviation possible*, Second edition. ed. (Airplane Stability & Control). Cambridge: Cambridge University Press, 2002.
- [14] A. W. Babister, *Aircraft stability and control*. New York, Oxford: Pergamon, 1961.
- [15] E. L. Goldsmith and I. McGregor, "The effect of shielding on the performance of a rectangular pitot intake at subsonics and supersonic speeds," RAE, Technical Report TR 88018, 1988.
- [16] E. L. Goldsmith and J. Seddon, *Practical intake aerodynamic design*. Oxford: Blackwell, 1993.
- [17] W. W. Rhoades and L. E. Surber, "Top-mounted inlet flow field testing for future fighter aircraft," *AIAA*, vol. 79, no. 1147, 1979.
- [18] F. Papadopoulos, I. Valakos, and I. K. Nikolos, "Design of an S-duct intake for UAV applications," *Aircraft Engineering*, vol. 84, no. 6, pp. 439-456, 2012, doi: 10.1108/00022661211272990.
- [19] J. M. Abbott, B. H. Anderson, E. J. Rice, and Nasa, "INLETS, DUCTS, AND NOZZLES," in *1987 Conf on Aeropropulsion*, Nasa, Lewis Res Ctr, Cleveland, Oh, Nov 17-19 1987, vol. 3049, in Nasa Conference Publication, 1990, pp. 157-174.
- [20] J. D. Anderson, *Fundamentals of aerodynamics*, Sixth edition. International student edition. ed. New York, N.Y.: McGraw-Hill Education, 2017.
- [21] Callen-Lenz, "Q&A with Callen-Lenz Team," C.-L. E. Team, Ed., ed, 2023.
- [22] R. H. Sundararaj, T. C. Sekar, R. Arora, and A. Kushari, "Effect of nozzle exit area on the performance of a turbojet engine," *Aerospace Science and Technology*, vol. 116, Sep 2021, Art no. 106844, doi: 10.1016/j.ast.2021.106844.
- [23] H. Schlichting and K. Gersten, *Boundary-Layer Theory*, 9th 2017. ed. Berlin, Heidelberg: Springer Berlin Heidelberg : Imprint: Springer, 2017.
- [24] D. B. Spalding, "A Single Formula for the "Law of the Wall"," *Journal of applied mechanics*, vol. 28, no. 3, pp. 455-458, 1961, doi: 10.1115/1.3641728.
- [25] A.-L. Delot, T. M. Berens, M. H. Tormalm, M. Säterskog, and N. Ceresola, "DES Computations for a Subsonic UAV Configuration with a Highly Integrated S-Shaped Intake Duct," in *52nd Aerospace Sciences Meeting*, 2014, doi: 10.2514/6.2014-0723. [Online]. Available: <https://arc.aiaa.org/doi/abs/10.2514/6.2014-0723>

- [26] H. K. Versteeg and W. Malalasekera, *An introduction to computational fluid dynamics : the finite volume method*, 2nd ed. Harlow: Pearson Prentice Hall, 2007.
- [27] M. Sosnowski, J. Krzywanski, K. Grabowska, and R. Gnatowska, "Polyhedral meshing in numerical analysis of conjugate heat transfer," in *12th International Conference on Experimental Fluid Mechanics (EFM)*, Mikulov, CZECH REPUBLIC, Nov 21-24 2017, vol. 180, in EPJ Web of Conferences, 2018, doi: 10.1051/epjconf/201818002096. [Online]. Available: <Go to ISI>://WOS:000454317800097
- [28] J. Blazek, *Computational fluid dynamics : principles and applications*, 2nd ed. Oxford: Elsevier, 2005.
- [29] P. J. Roache, *Computational fluid dynamics*. Albuquerque, N.M.: Hermosa, 1976.
- [30] D. G. MacManus, N. Chiereghin, D. G. Prieto, and P. Zachos, "Complex Aeroengine Intake Ducts and Dynamic Distortion," *AIAA Journal*, vol. 55, no. 7, pp. 2395-2409, 2017, doi: 10.2514/1.J054905.
- [31] B. D. J. Schreiner, "Computational Modelling of Gas Turbine Aerodynamics with Endwall Contouring," Thesis (PhD) - University of Bath, Bath, 2020.
- [32] S. B. Pope, *Turbulent flows*. Cambridge: Cambridge University Press, 2000.
- [33] "Inlet Total-Pressure-Distortion Considerations for Gas-Turbine Engines," Soc. of Automotive Engineers, Warrendale, PA, Soc. of Automotive Engineers Rept. 1419a, 1999.
- [34] C. Lee and C. Boedicker, "Subsonic diffuser design and performance for advanced fighter aircraft," in *Aircraft Design Systems and Operations Meeting*, 1985.
- [35] S. Qiu, H. Liu, and W. P. Li, "Turbofan duct geometry optimization for low noise using remote continuous adjoint method," in *Proceedings of the Institution of Mechanical Engineers Part C-Journal of Mechanical Engineering Science*, Jan 2015, vol. 229, no. 1, pp. 69-90, doi: 10.1177/0954406214532631. [Online]. Available: <Go to ISI>://WOS:000347163900007

APPENDICES

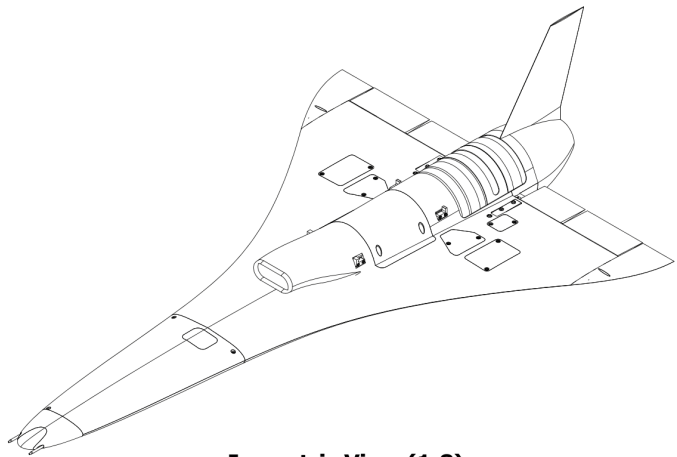
3.1 Appendix A – Turbojet Decision Matrix

Company	JetCat							Behotec	
Model	P220	P250	P300	P400	P500	P550	P1000	B300	B350*
F/D ()	1.22	1.44	1.39	1.32	1.41	1.52	1.35	1.43	1.57
F/A (N/m^2)	0.0149	0.0164	0.0165	0.0173	0.0159	0.0172	0.0175	0.0162	0.0178
F/W ()	22.3	26.3	24.8	22.4	23.4	25.3	20.5	25.5	28.0
Cost (£)	4880	4125	4425	9695	12500	13750	25000	4845	6928

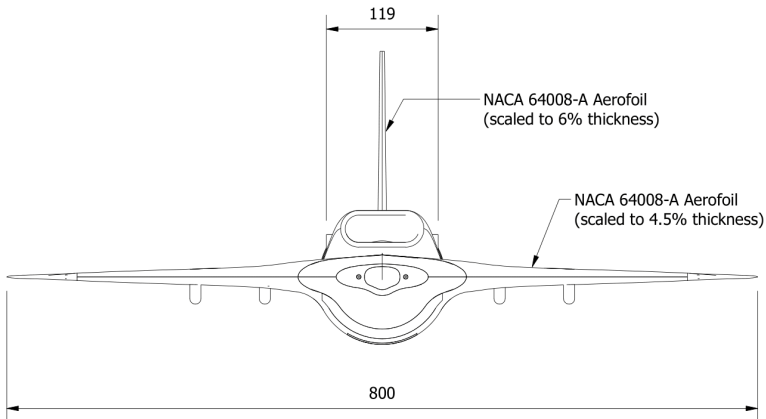
*The Behotec B350 is unreleased and based on the same platform as the B300, in the same way the JetCat P500 and P550 are. Its performance has been estimated using the same percentage change in parameters as between the JetCat P500 and P550.

3.2 Appendix B - General Assembly Drawing

See overleaf for a General Assembly of the aircraft from [1].



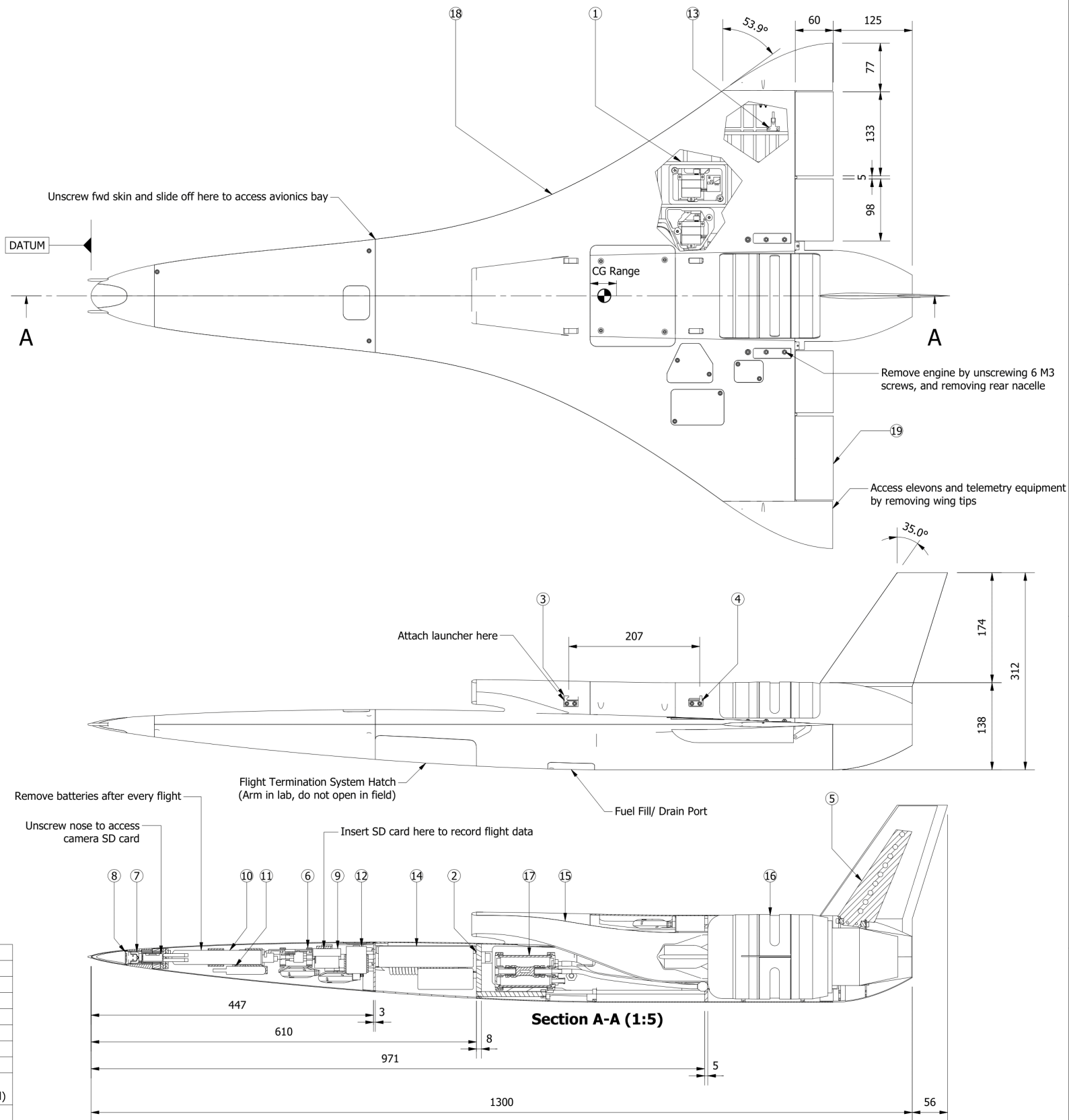
Isometric View (1:8)

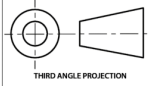



PARTS LIST				
REF	NUMBER	NAME	QTY	TYPE
-	KF-ST-01(L)	Internal Wing Structure - Left	1	Sub-assembly
1	KF-ST-01(R)	Internal Wing Structure - Right	1	Sub-assembly
2	KF-ST-02	Central Fuselage Structure	1	Sub-assembly
3	KF-ST-02-005	Front Launcher Mount	2	Part
4	KF-ST-02-006	Rear Launcher Mount	2	Part
5	KF-ST-03	Rear Fuselage Structure	1	Sub-assembly
6	KF-ST-04	Avionics Bay	1	Sub-assembly
7	KF-ST-05	Nose & Ballast	1	Sub-assembly
8	KF-ST-05-001	FPV Camera	1	Part
9	KF-AV-01	Main Avionics	1	Sub-assembly
10	KF-AV-01-001	4000mAH Gensace LIPO Battery	1	COTS Component
11	KF-AV-01-002	450mAH Gensace LIPO Battery	1	COTS Component
12	KF-AV-01-003	Laser Altimeter	1	COTS Component
13	KF-AV-02	Telemetry System	1	Sub-assembly
14	KF-FT-01	Parachute System	1	Sub-assembly
15	KF-PR-01	Propulsion System	1	Sub-assembly
16	KF-PR-01-001	Jetcat P300 Pro Jet Engine	1	COTS Component
17	KF-PR-02	Fuel System	1	Sub-assembly
18	KF-AE-01	Fibreglass Skin	1	Sub-assembly
19	KF-AE-02(L)	Elevon System - Left	1	Sub-assembly
-	KF-AE-02(R)	Elevon System - Right	1	Sub-assembly

KEY PARAMETERS	
PARAM	VALUE
Max Take-off Weight	10.8 kg
Empty Weight	9.5 kg
Fwd CG Limit	795mm from DATUM
Aft CG Limit	835mm from DATUM
Maximum Fuel Capacity	1.76 L
Fuel	Synthetic Kerosene
Max. Speed Level	616 mph (Mach 0.81 @sea level)
Landing Speed	25 m/s (20° alpha)

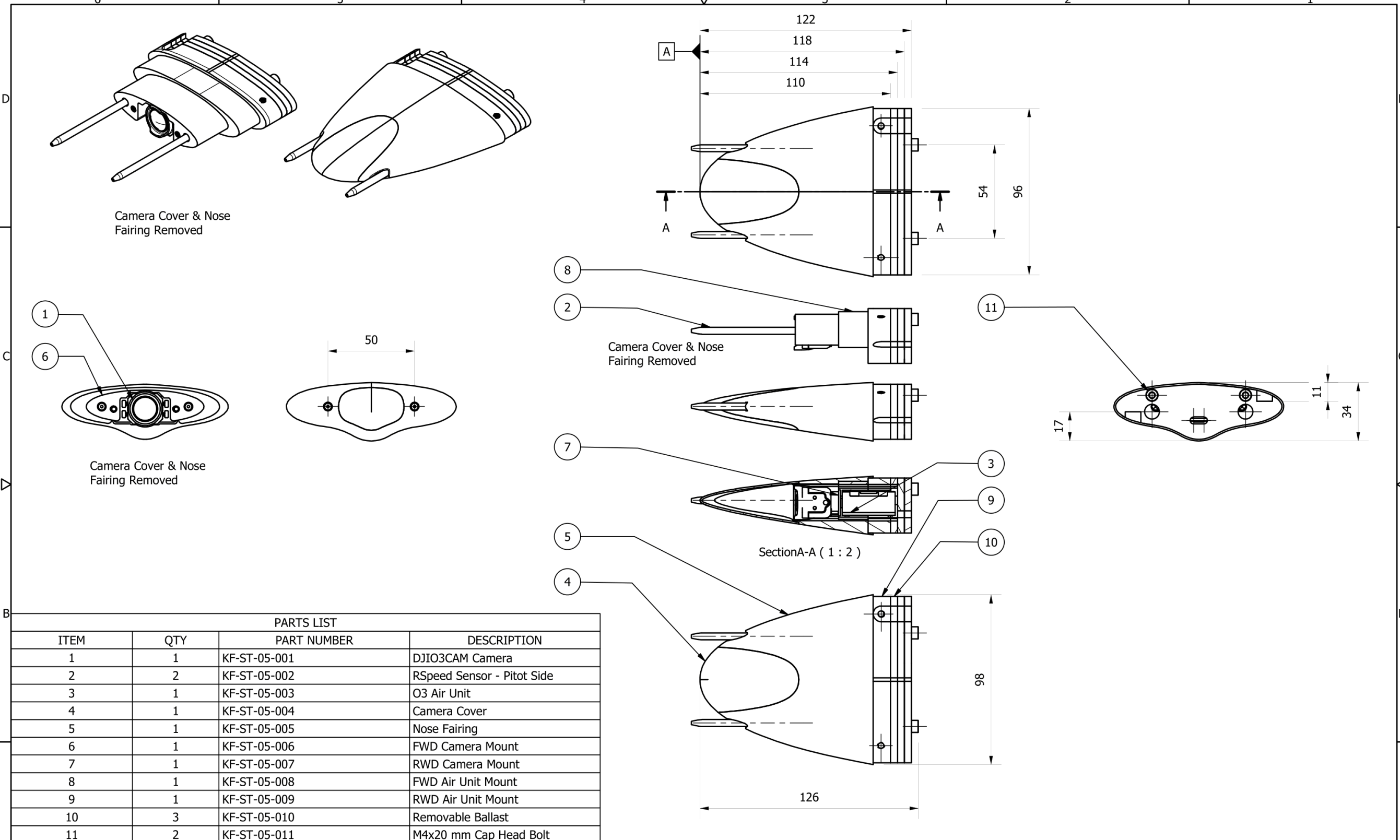
AERODYNAMIC PARAMETERS		
PARAM	MAIN WING	TAIL
Effective Area	0.3 m ²	0.02 m ²
Leading Edge Sweep	53.9° - 85.1°	35°
Trailing Edge Sweep	0°	26.9°
Thickness	4.5%	6%
Reference Aerofoil	NACA 64008A	NACA 64008A



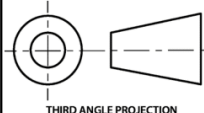

DO NOT SCALE: IF IN DOUBT, PLEASE ASK.		TOLERANCES UNLESS OTHERWISE STATED: LINEAR 0dp ± 0.25mm ; 1dp ± 0.1mm; 2dp ± 0.05mm		ANGULAR ± 0.5° (30')	
ALL DIMS. IN MM SCALE: 1 : 5	Contact Details: djs90@bath.ac.uk	Remove all sharp edges. Ro. 0,8 unless stated	Designed by Daniel Sykes	Checked by	Approved by
		© UNIVERSITY OF BATH THIS DOCUMENT IS COPYRIGHT AND THE PROPERTY OF THE UNIVERSITY OF BATH. IT MUST NOT BE COPIED IN WHOLE OR IN PART NOR DISCLOSED TO ANY THIRD PARTY WITHOUT PRIOR PERMISSION OF THE UNIVERSITY		Date	Sheet size
				15/05/2023	A2
Department of Mechanical Engineering				TITLE: Mach Initiative - Kingfisher General Assembly	
PART No. KF-01		Edition 3		Sheet 1 / 1	

3.3 Appendix C - Nose & Ballast Sub-Assembly Drawing

See overleaf for the Nose & Ballast Sub-Assembly.

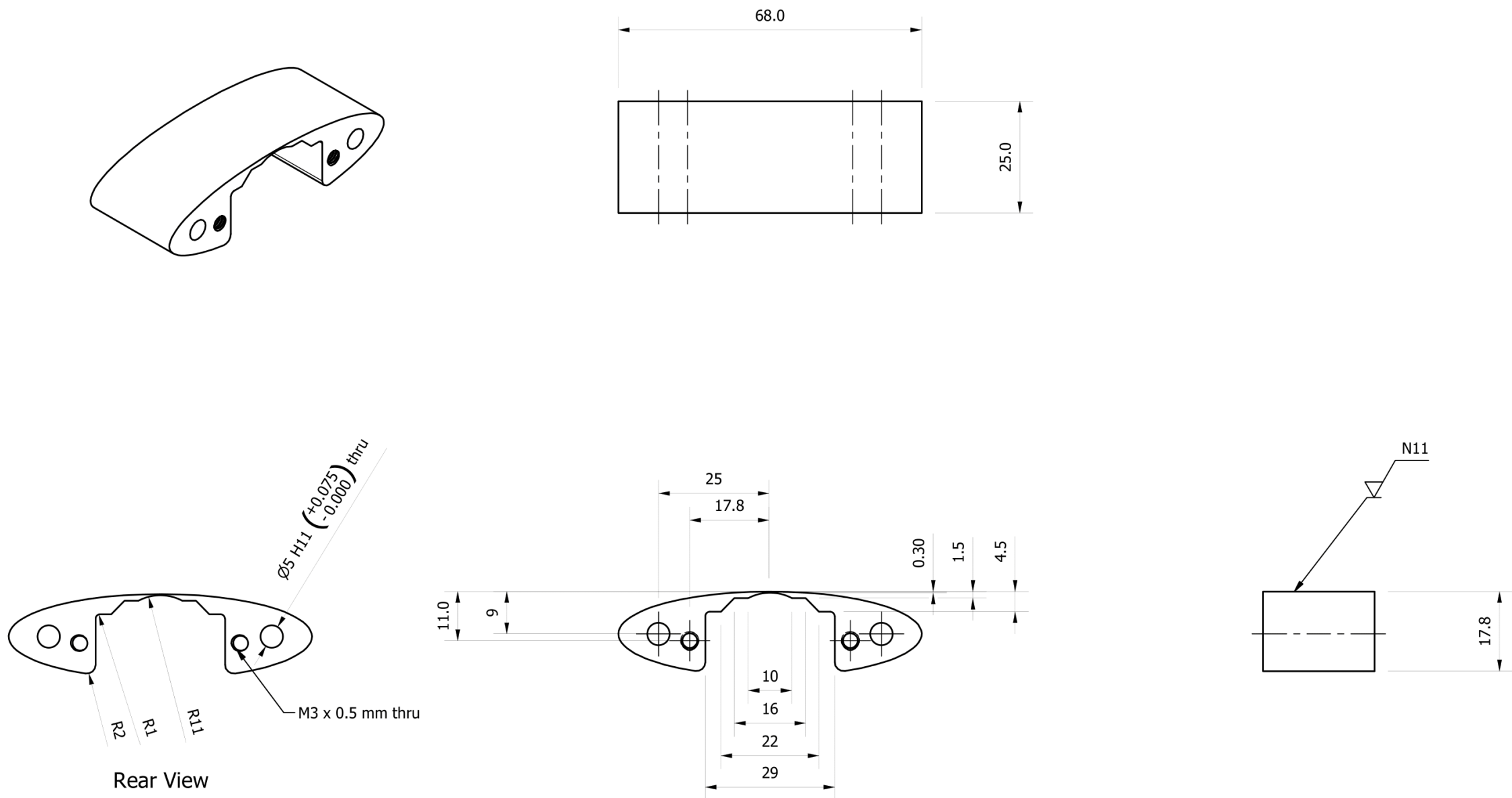


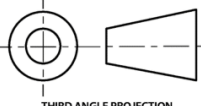

PARTS LIST			
ITEM	QTY	PART NUMBER	DESCRIPTION
1	1	KF-ST-05-001	DJIO3CAM Camera
2	2	KF-ST-05-002	RSpeed Sensor - Pitot Side
3	1	KF-ST-05-003	O3 Air Unit
4	1	KF-ST-05-004	Camera Cover
5	1	KF-ST-05-005	Nose Fairing
6	1	KF-ST-05-006	FWD Camera Mount
7	1	KF-ST-05-007	RWD Camera Mount
8	1	KF-ST-05-008	FWD Air Unit Mount
9	1	KF-ST-05-009	RWD Air Unit Mount
10	3	KF-ST-05-010	Removable Ballast
11	2	KF-ST-05-011	M4x20 mm Cap Head Bolt

DO NOT SCALE: IF IN DOUBT, PLEASE ASK.		TOLERANCES UNLESS OTHERWISE STATED: LINEAR 0dp \pm 0.25mm ; 1dp \pm 0.1mm; 2dp \pm 0.05mm ANGULAR \pm 0.5° (30')							
ALL DIMS. IN MM SCALE: 1 : 2	Contact Details: rjt67	Remove all sharp edges. Ro. 0,8 unless stated	Designed by Romesh Thayalan	Checked by	Approved by	Date 19/05/23	Sheet size A3	Date 19/05/2023	PROJECT MACH
 THIRD ANGLE PROJECTION		© UNIVERSITY OF BATH THIS DOCUMENT IS COPYRIGHT AND THE PROPERTY OF THE UNIVERSITY OF BATH. IT MUST NOT BE COPIED IN WHOLE OR IN PART NOR DISCLOSED TO ANY THIRD PARTY WITHOUT PRIOR PERMISSION OF THE UNIVERSITY			Department of Mechanical Engineering		 UNIVERSITY OF BATH		TITLE: Nose & Ballast Sub-Assembly
					PART No. KF-ST-05		Edition	Sheet 1 / 1	

3.4 Appendix D - FWD Camera Mount Part Drawing

See overleaf for the FWD Camera Mount Part Drawing.



DO NOT SCALE: IF IN DOUBT, PLEASE ASK.		TOLERANCES UNLESS OTHERWISE STATED: LINEAR 0dp ± 0.25mm ; 1dp ± 0.1mm; 2dp ± 0.05mm							ANGULAR± 0.5° (30')	
ALL DIMS. IN MM SCALE: 1 : 1	Contact Details: rjt67	Remove all sharp edges. Ro. 0,8 unless stated	Designed by Romesh Thayalan	Checked by	Approved by Date 22/05/23	Sheet size A3	Date 22/05/2023	PROJECT MACH		
 THIRD ANGLE PROJECTION	© UNIVERSITY OF BATH THIS DOCUMENT IS COPYRIGHT AND THE PROPERTY OF THE UNIVERSITY OF BATH. IT MUST NOT BE COPIED IN WHOLE OR IN PART NOR DISCLOSED TO ANY THIRD PARTY WITHOUT PRIOR PERMISSION OF THE UNIVERSITY Department of Mechanical Engineering  UNIVERSITY OF BATH				TITLE: FWD Camera Mount					
					PART No. KV-ST-05-006		Edition	Sheet 1 / 1		